Theoretical modelling of nano-structured (Hf,Zr)N/(Sc,Y)N metal/semiconductor superlattices for thermoelectric energy conversion

A thesis submitted in partial fulfilment
for the degree of Master of Science as a part
of the Integrated Ph.D programme
(Materials Science)

By

Bivas Saha

Chemistry and Physics of Materials Unit

Jawaharlal Nehru Centre for Advanced Scientific Research

Bangalore-560064

(A Deemed University)

April 2010

To my family

DECLARATION

I hereby declare that the matter embodied in the thesis entitled “**Theoretical modelling of nano-structured (Hf,Zr)N/(Sc,Y)N metal/semiconductor superlattices for thermoelectric energy conversion**” is the result of investigations carried out by me at the Chemistry and Physics of Materials Unit, Jawaharlal Nehru Centre for Advanced Scientific Research, Bangalore, India under the supervision of Prof. Umesh V. Waghmare and that it has not been submitted elsewhere for the award of any degree or diploma.

In keeping with the general practice in reporting scientific observations, due acknowledgement has been made whenever the work described is based on the findings of other investigators.

Bivas Saha

CERTIFICATE

I hereby certify that the matter embodied in this thesis entitled “**Theoretical modelling of nano-structured (Hf,Zr)N/(Sc,Y)N metal/semiconductor superlattices for thermoelectric energy conversion**” has been carried out by Mr. Bivas Saha at the Chemistry and Physics of Materials unit, Jawaharlal Nehru Centre for Advanced Scientific Research, Bangalore, India under my supervision and that it has not been submitted elsewhere for the award of any degree or diploma.

Prof. Umesh V. Waghmare
(Research Supervisor)

Acknowledgements

"Change your orbit, constantly! despite of all odds and difficulties. It is the key to our progress as an individual and as a nation"

Today, at the moment of this thesis submission, I am happy and glad that once again in my life, I am changing an orbit, and entering into another with new challenges, opportunities, and hope. Let me take this opportunity to thank all those people who have shaped my life and my career, and made me eligible to write this thesis.

First among those is undoubtedly is my thesis adviser Prof. Umesh V. Waghmare. He taught me how to do science. His sheer enthusiasm for science, and drive for perfections have always envy me. I am and will always be deeply indebted to him for all the suggestions, discussions, and encouragement to be self dependent. He will always remain my adviser and my philosopher.

I wish to express my gratitude to all the JNCASR professors, especially Prof. S. K. Pati, Prof. S. Balasubramanian, Prof. A. Sundaresan, Prof. C. Narayana, Prof. K. S. Nanayan, Prof G. U. Kulkarni, Prof. S. M. Shivaprasad, Prof**.** S. Ranganathan, Prof. S. Narasimhan, Dr. S. K. Das, Dr. N. S. Vidyadhiraja, Dr. T. K. Maji, Dr. M. Eswaramoorthy and others. I have benefitted immensely not only from their class courses, but also from the scientific discussions that I had with them.

I would also like to thank Prof. Timothy D. Sands, whose experimental work has motivated me to undertake the project presented in this thesis. He has been kind and generous to me, and my ideas. He holds a special place in my heart.

Let me also thank all my other collaborators, Prof. Timothy Fisher, Prof. Mark Lundstrom, Dr. Stuart Parkin, Dr. Ricardo Grau-Crespo, Dr. Murali Kota, Jagaran Acharya, Nelson Yaw Dzade, Changwook Jeong, Robert Wortman, Joseph Feser, Zehn Huang. I had fruitful and exciting discussions with them, and I thank all of them for being so kind and polite to me.

I am grateful to all the computing facilities such as Octopus, Octagon, Hexagon, and Sampige. They are the ones, on whose shoulder I am writing this thesis.

I would like to thank Prof. C N R Rao and Prof. M R S Rao for building JNC as a world class research institute, with world class research facilities.

I am also thankful to all my batch mates of the Int. Phd. 2007 batch. I specially thank Soumik, with whom I have not only shared room in first year, but also we were course laboratory partners, and Movie club members. I would also like to thank Ritu, and Abhay for being such a wonderful friend. We have spent a lot of time together, and they will always have a special place in my heart. All my other batch mates Nitesh, Piyush, Sekhar, Vini, Urmi, Nisha are great, and I have enjoyed being with them.

I would also like to thank all my lab members. Very special thanks to Hembram, who helped me in all possible ways that he could have. I would also like to thank Anil, Arun, Sandeep, Jagaran, Nelson, Sampson, Soumya, Sharmila, Deepashri, Sumant, Dev, Srijan, Niladri, Puskal, Manoj, Anirban, Abhishek, Alok, Kaushalendra, Shailendra, Satadeep, Asha, Mousumi, and Anitha.

I would also like to thank all members of my junior Int. Ph.D. batches, all my friends in JNC including Dinesh, Dhiraj, Prakash, Partho, Sudipta, Sudip and others for making my stay at JNC comfortable.

I thank all the complab members Ravi, Dharma, Vikas, Nisaz, and others. I would like also like to thank Sukanya Mam, and Princy Mam from academic section for all the helps.

Finally, I wish to thank Kabita for being such a wonderful friend of mine over the years. Her constant support, enthusiasm and love have always been my guiding force.

Contents

1. Introduction

2. Bulk Nitride Materials (ZrN, HfN, and ScN): Electronic structure, vibrational spectra and thermal properties

3. Electronic structure, vibrational spectrum and thermal properties of YN: A first-principles study

3.3 Results

4. Thermoelectric properties of ZrN/ScN and HfN/ScN metal/semiconductor superlattices

4.3 Results

.

My other works at JNCASR

Thermoelectric materials

1. Elastic constants of ZrN/ScN and HfN/ScN metal/semiconductor superlattices.

2. Thermoelectric properties of **strained** ZrN/ScN and HfN/ScN metal/semiconductor superlattices.

3. Full band vs. effective mass treatment of thermoelectric transport coefficients of nitride metal/semiconductor superlattices. (*In collaboration with Changwook Jeong, and Prof. Mark Lundstrom, Purdue University*.)

4. Estimation of thermal boundary resistance of (Hf,Zr)N/(Sc,Y)N superlattices using diffuse mismatch model. (*In collaboration with Joseph Feser, University of California, Berkeley*.)

Molecular Thermoelectric Materials

1. Modeling thermal transport at the molecular hetero-junctions: A density functional theory and atomistic Greens function study. (*In collaboration with Nelson Yaw Dzade (JNCASR), and Prof. Tim Fisher (Purdue University)*)).

Spintronic Materials

1. Modeling dilute magnetic semiconductors (DMS) based on MgO systems. (*In collaboration with Dr. Ricardo Grau-Crespo, (University college, London), Dr. Murali Kota (IBM, India), and Dr. Stuart Parkin (IBM, US).*)

SYNOPSIS

Thermoelectric materials that convert heat flux into electrical energy are a topic of great scientific interest because of their potential to deal with the present day energy challenges. Wide range applications and commercialization of these materials though critically depends on our ability to improve their efficiency by at least two to three folds from the present day laboratory value.

The present thesis work deals with modelling how electrons and phonons behave in nano-structured metal/semiconductor superlattices based on (Hf,Zr)N/(Sc,Y)N system, using first-principles density functional theory based calculations. Electronic structure, vibrational spectra, and thermal properties of these nitrides in bulk form are determined. The superlattices, made of these nitrides are simulated to understand their potential and suitability for thermoelectric applications.

The first chapter of the thesis provides a brief introduction to thermoelectric materials, and related research. Starting from basic concepts like Seebeck and Peltier effect, we have invoked modern concepts like Mahan & Sofo theory, and Boltzmann transport theory to present the theoretical basis of advanced thermoelectric materials. The conflicting design challenges that prevent us from developing highly efficient thermoelectric materials are also discussed. Insightful pictures about the metal/semiconductor superlattices are given, and their working principle is discussed.

In the second chapter, we present the electronic structure, vibrational spectra, and thermal properties of bulk ScN, ZrN, and HfN. Hubbard U correction is used to fit the band gap with the experimental values and to connect it with the transport related effective mass calculations. Vibrational spectra, lattice specific heat, and lattice thermal conductivity are also estimated to understand their potential to be used as component materials for metal/semiconductor superlattices.

In the third chapter, we have used a combination of (1) generalised gradient approximation (GGA), (2) A Hubbard U correction along with GGA, and (3) GW approximation to estimate band gaps, effective masses, and volume deformation potentials of YN. Vibrational spectra, and thermal properties are estimated to understand its potential and suitability for alloying with other nitrides for thermoelectric applications.

The last chapter of this thesis contains extensive theoretical analysis of ZrN/ScN and HfN/ScN metal/semiconductor superlattices for thermoelectric applications. The crystal structure, interface energy density, and inter planer distances are discussed. Electronic structures of these superlattices

are calculated, and enhancement of Seebeck coefficient along the growth direction is discussed. Vibrational spectrum, lattice thermal conductivity, and its dependence on temperature, and contribution of phonons as a function of frequency is analysed. Finally we comment on the relative superiority of HfN based systems over ZrN ones.

List of Tables

List of Figures

Chapter 1

Introduction

An ever growing demand for alternate clean, green energy, coupled with climate change is bringing dramatic changes in the social and political structure of the world. The solution to this grand challenge lies essentially on discovering new and alternate source of energy, minimizing our over dependence on fossil fuel and conventional energy sources like coal and oil. Thermoelectric materials that convert heat flux directly into electrical energy hold an enormous promise to partly deal with this great challenge, and have been a topic of renewed scientific interest. These materials are characterised by their thermoelectric figure of merit $ZT = \frac{S^2\sigma}{\kappa_e+\kappa_p}T$, where S is the Seebeck coefficient, σ is the electrical conductivity, κ_e and κ_p are electronic and phonon contribution to thermal conductivity respectively, and T is the operating temperature. To be competitive with conventional power generator and refrigerator, we must develop materials with ZT of the order of 3-4, however research with conventional bulk materials in the last half century has yielded materials with ZT of the order of 1. Recent development in nano-science and nano-engineering has demonstrated a possibility of increasing ZT, and many of the efforts in thermoelectric are now devoted in this direction.

1.1 History and current status of thermoelectric energy research

History of thermoelectricity and thermoelectric materials dates way back to the days of Johann Seebeck (1822) and Peltier (1834), for their pioneering discovery of Seebeck effect and Peltier effect respectively. But it is W. Thomson who provided the first important theoretical basis for thermoelectricity. He related, mathematically, the Peltier and Seebeck effects and predicted the existence of the Thomson effect.

The first practical thermoelectric material was developed in USSR during the World War II to power radio sources. And in the mid fifties discoveries were made regarding materials which expanded the potential applications of this technology by opening up the possibilities to use larger temperature differences and higher efficiencies.

Most of the early thermoelectric materials were based on the electron crystal phonon glass type materials like Bi_2Te_3, PbTe and its alloys, whose electrical properties are in the higher side like that of electron crystal, while thermal conductivity are of the order of phonon glass. But with the best of effort one could reach ZT of the order of 1 with these conventional materials, which the practical demand to achieve ZT about 3-4 remained elusive, and essentially no break-through happened from sixties to eighties.

Figure 1(a)

Figure 1(b)

Figure 1 (a) Schematic diagram of a thermoelectric device operating over a temperature gradient (http://web.mit.edu/nanoengineering/). (b) A prototype of real life thermoelectric device used by NASA for its space science exploration (http://thermoelectrics.caltech.edu/).

The development of nano-science and nano-engineering in early nineties rejuvenated the field. The pioneering work of Dresselhaus and Hicks[1,2] showed for the first time that nano-structured materials have immense potential to increase the material's thermoelectric performance. Their one-band model predicted that one dimensional nano-wire, two dimensional superlattices will have larger figure of merit due to the quantum confinement of electron and phonon. Their predictions were subsequently realised experimentally by Venkatsubramian et al[3] and Harman et al[4]. While Venkatsubramian et al used Bi_2Te_3/Sb_2Te_3 superlattice to increase ZT upto 2.4, Harman et al investigated PbSeTe/PbTe quantum dot superlattice. Most of this enhancement of ZT was due to the reduction in lattice thermal conductivity coming from the quantum confinement of phonons at the interface of superlattices.

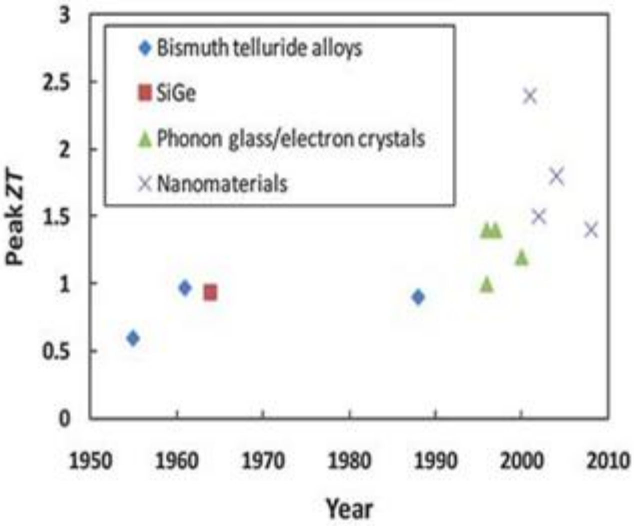

Figure 2. Historical development of thermoelectric materials efficiency[3].

In the meantime, better theoretical understanding of thermoelectric energy transport gave a new dimension to the bulk thermoelectric energy research, with Kanatzidis and Snyder taking lead. Kanatzidis et al[6] found ZT_{max} about 2.2 at 800 K in $AgPb_mSbTe_{2+m}$, while Snyder et al[7] used density of states engineering to increase ZT about 1.6 for p-type PbTe. The increase in ZT of these materials can be attributed to large mass of the constituent atoms, and heavy unit cell, reducing the lattice thermal conductivity without hampering the electrical properties. Although promising for their relatively easy manufacturability compared to the nano-structured superlattices, the presence of poisonous Pb may however restrict their practical application.

Thermoelectric materials research today also circles around these two regimes (1) Nano-structured materials, like superlattices, quantum wires etc, and (2) Bulk materials with heavy atoms, and doping. Metal/semiconductor superlattices are currently being explored at various groups for their potential increment in ZT. The present thesis contains some important theoretical modelling results of two promising metal/semiconductor superlattices namely ZrN/ScN and HfN/ScN which are currently being investigated experimentally by a group of scientist at the Purdue University [Tim Sands et al.].

1.2 Basics of Thermoelectricity

1.2.1 Seebeck effect

The **Seebeck effect** is the conversion of temperature difference directly into electricity.

Seebeck in 1822 observed that if a temperature difference exists between two dissimilar metals or semiconductors, an electrical current flow in the closed loop formed by the constituents' elements. The voltage produced is proportional to the temperature difference between the two junctions, and the proportionality constant is known as the Seebeck coefficient, and often referred to as the thermoelectric power or thermopower.

$$V = a(T_h - T_c) \tag{1}$$

The voltage difference, V, produced across the terminals of an open circuit made from a pair of dissimilar metals, A and B, whose two junctions are held at different temperatures, is directly proportional to the difference between the hot and cold junction temperatures, T_h - T_c.

1.2.2 Peltier effect

Peltier effect represents the calorific effect of an electrical current at the junction of two different metals. Peltier in 1834 discovered that When a current I is made to flow through the circuit, heat is released at the upper junction (at T_2), and absorbed at the lower junction (at T_1). The Peltier heat absorbed by the lower junction per unit time, $\dot{Q}$ is equal to

$$\dot{Q} = \Pi_{\mathrm{AB}} I = (\Pi_{\mathrm{B}} - \Pi_{\mathrm{A}})\, I \tag{2}$$

where, I is electrical current and Π_{AB} is the Peltier coefficient of the materials.

1.2.3 Thomson effect

The **Thomson effect** was predicted and subsequently experimentally observed by Thomson in 1851. It describes the heating or cooling of a current-carrying conductor with a temperature gradient. Any current-carrying conductor (except for a superconductor), with a temperature difference between two points, will either absorb or emit heat, depending on the material.

If a current density J is passed through a homogeneous conductor, heat production per unit volume is:

$$q = \rho J^2 - \mu J \frac{dT}{dx} \tag{3}$$

where ρ is the resistivity of the material, dT/dx is the temperature gradient along the wire, μ is the Thomson coefficient.

1.3 Figure of merit of thermoelectric materials and conflicting design challenges

The figure of merit of a thermoelectric device is defined as

$$ZT = \frac{S^2\sigma}{\kappa_e + \kappa_p} T \tag{4}$$

Where S is the Seebeck Coefficient, σ is the electrical conductivity, κ_e and κ_p are electronic and phonon contribution to thermal conductivity respectively, and T is the operating temperature or average temperature. Higher the value of ZT, better the material is for thermoelectric applications.

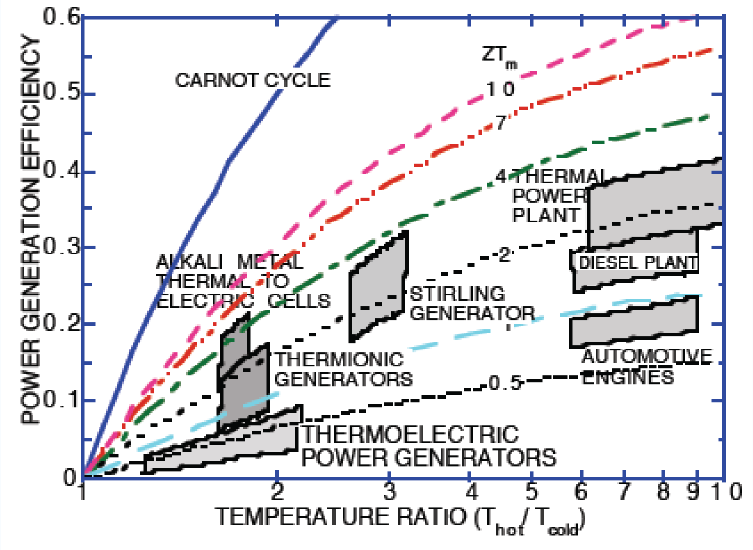

Figure 3. Thermoelectric power generation efficiency compared with other conventional power sources at different temperature ratio[8].

Figure 3 shows comparison of thermoelectric power generation efficiency of different processes. The thermal power plant and diesel plant has much higher power generation efficiency than thermoelectric materials, which stands way low. So, to be competitive with these power sources we must develop materials with ZT of the order of 3-4. But it is not easy to increase ZT because of the presence of mutually conflicting design parameters in the ZT expression

(a). If one increases the electrical conductivity (σ) by increasing the carrier concentration (n) [see expression 5], then according to Mott equation [see expression 6] of Seebeck coefficient (S) goes down.

$$\sigma = \frac{ne^2\tau}{m^*} \qquad (5)$$

$$S = \frac{8\pi^2 k_B^2 T}{3eh^2} m^* \left(\frac{\pi}{3n}\right)^{\frac{2}{3}} \qquad (6)$$

(b). Moreover because of Wideman Franz law increase in electrical conductivity (σ) will be accompanied by increase in electronic contribution to thermal conductivity (κ_e).

(c). Increase in effective mass of the system will increase the Seebeck coefficient (S), but the electrical conductivity (σ) will then go down.

(d). Artificial creation of defects will reduce the lattice contribution to thermal conductivity, but it also adversely affects the electrical conductivity.

Although the creation of a more efficient thermoelectric material is an optimisation problem between S, $\sigma, and\ \kappa$, it is hard to optimise all in order to get a high ZT.

1.4 Mahan & Sofo theory

In an article titled "The best thermoelectric", Mahan and Sofo[9] came up with an elegant theoretical understanding of thermoelectricity. They solved the Boltzmann transport equation under relaxation time approximation to get expressions for electrical conductivity, Seebeck coefficient, and electronic contribution to thermal conductivity. Their expressions for these properties are

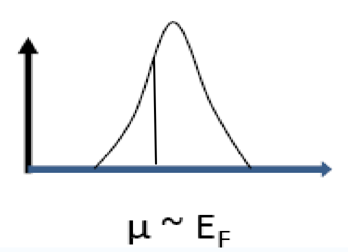

$$\sigma = e^2 \int_{-\infty}^{+\infty} d\varepsilon \, (-\frac{df_0}{d\varepsilon})\Sigma(\varepsilon) \quad (7)$$

$$T\sigma S = e \int_{-\infty}^{+\infty} d\varepsilon \left(-\frac{df_0}{d\varepsilon}\right)\Sigma(\varepsilon)(\varepsilon-\mu) \qquad (8)$$

$$T\kappa_e = \int_{-\infty}^{+\infty} d\varepsilon \, (-\frac{df_0}{d\varepsilon})\Sigma(\varepsilon)(\varepsilon-\mu)^2 \quad (9)$$

where $\sigma, S, and\ \kappa_e$ are electrical conductivity, Seebeck coefficient, and electronic contribution to thermal conductivity respectively, $f_0\ is\ the$ Fermi-Dirac distribution function, μ is the chemical potential of a material under consideration, and $\Sigma(\varepsilon)$ is the transport distribution function, given by

$$\Sigma(\varepsilon) = \sum_k v_x(k)^2\, \tau(k)\delta(\varepsilon - \varepsilon(k)) \quad (10)$$

where $v_x(k)$ is the group velocity of electron along x-direction, and having a wave-vector k, $\tau(k)$ is the relaxation time of the electron, and $\delta(\varepsilon - \varepsilon(k))$ is the density of states.

The first derivative of the Fermi-Dirac distribution function is bell-shaped in nature, and cantered around the Fermi energy.

It is clear from the expression 9 that to achieve high Seebeck coefficient one need to have an asymmetry in the density of states at the Fermi energy, so which gives a large first moment $(\varepsilon - \mu)$, and maximum thermopower. This is a key requirement of any type of thermoelectric materials.

1.5 Expression of lattice thermal conductivity

Boltzmann transport equation which works well in the quasi-ballistic regime can also be solved to obtain an expression for lattice thermal conductivity, which looks similar to its electronic counterpart, with the only difference that we now have Bose-Einstein distribution function, rather than Fermi-Dirac distribution. The expression is shown below.

$$\kappa = \hbar \sum_\lambda \int \frac{d^3q}{(2\pi)^3}\ v_{z\lambda}(q)^2 \omega_\lambda\ (q)\tau_\lambda(\mathrm{q})(\frac{dn_B[\omega_\lambda(q)]}{dT}) \qquad (11)$$

$n_B[\omega_\lambda(q)]$ is the Bose-Einstein distribution function, $\omega_\lambda(q)$ is the frequency of the phonon having q wave vector and λ normal mode.

1.6 Metal/semiconductor superlattices

Because of mutually conflicting design challenges mentioned above, it is very hard to achieve ZT above 2 till today. No conventional metal or semiconductors has the potential it seems, to live up to the expectations of having a high ZT. One approach which is currently being explored and which has a lot of potential is metal/semiconductor superlattices[10]. Effective energy filtering mechanism at the interface of the superlattices by creation of optimum Schottky barriers heights, as well as reduced lattice thermal conductivity resulting from the mismatch of phonon density of states at the interface does give higher ZT in these materials.

Superlattices are periodic layers of different materials stacked one after another, where the periodicity may vary from nano to micro range. Metal/semiconductor binary superlattices are formed by stacking one layer of metal on top of one layer of semiconductor and repeating the process [see Fig 5 (a)].

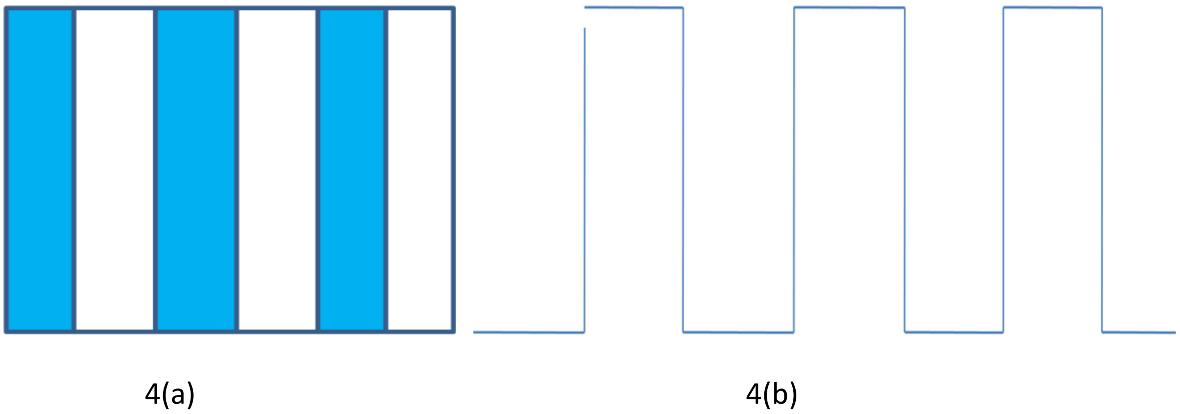

Figure 4 (a) Real space schematic diagram of a metal/semiconductor superlattice, (b) Reciprocal space picture. While the metallic layers act as potential well for electronic motion, the semiconductor layers offer barriers for its motion.

The metallic layers are represented as the quantum well, while semiconductor layers act as barriers to the low energy electrons. As a result only a certain fraction of the total conduction electron reaches from the hot side to the cold side, increasing the Seebeck coefficient of the materials. This selective transport of electron from the hot to the cold side is termed as the energy filtering mechanism, which plays a key role on the performance of these materials system.

Other advantage of these engineered materials engineering is, because of the mismatch in phonon density of states of the metal and the semiconductor, large number of phonons will get scattered at the interface, which will reduce the lattice thermal conductivity along the cross-plane directions.

Since traditionally reduction in lattice thermal conductivity has given highly efficient thermoelectric materials, the superlattices whose lattice thermal conductivity is more than 10-100 times lower than their individual bulk component may prove an efficient way of getting better efficiency.

However, drawback that these materials may have is its lower electrical conductivity because of the presence of the Schottky barriers, which may adversely affect the overall ZT.

1.7 Summary of the systems studied in the thesis

This thesis is aimed at gaining an insightful theoretical understanding of the physical and chemical properties of nitride metal/semiconductor superlattices for their potential application in the thermoelectric and thermionic energy conversion devices. We have attempted to (1) understand the role of electronic structure, vibrational spectra, and thermal properties of nitride materials, and their metal/semiconductor superlattices on their thermoelectric properties, (2) understand the role of epitaxial strain and interfaces on their transport properties, and (3) developing models that can be applied for superlattices with larger periodicities which are not simulated here. For each system of study (ZrN/ScN, and HfN/ScN), we have tried to point out how our results can be used for basic understanding and lead to technological applications.

References

1. L. D. Hicks and M. S. Dresselhaus, Phys. Rev. B, 16631, **47** (1993).

2. L. D. Hicks and M. S. Dresselhaus, Phys. Rev. B, 12727, **47** (1993).

3. R. Venkatasubramanian, E. Siivola, T. Colpitts, B. O'Quinn, Nature, **597** (2001).

4. T. C. Herman et al, Science, 2229, **297 (**2002).

5. J. Baxter et al, Energy and Environmental Science, 559, **2** (2009).

6. Hsu et al, Science, 303, **818** (2004).

7. Heremans et al, Science, 321, **554** (2008).

8. Gang Chen et al, Intl. Mater. Rev., 48, **45** (2003).

9. G. Mahan and Sofo, PNAS, 7436, **93 (**1996).

10. D. Vashaee and A. Shakouri, Phys. Rev. Lett., 106103, **92** (2004).

Chapter 2

Bulk Nitride Materials (ZrN, HfN, and ScN): Electronic structure, vibrational spectra and thermal properties

Abstract

With a motivation to understand microscopic aspects of ScN, ZrN, and HfN relevant to the thermoelectric properties of nitride metal/semiconductor superlattices, we determine their electronic structure, vibrational spectra and thermal properties using first-principles calculations based on density functional theory with a generalized gradient approximation of the exchange correlation energy. We find a large energy gap in the phonon dispersions of metallic ZrN and HfN, but a gapless phonon spectrum for ScN spanning the same energy range; this suggests that a reduced thermal conductivity, suitable for thermoelectric applications, should arise in superlattices made with ScN and ZrN or ScN and HfN. To obtain an electronic energy band gap of ScN comparable to experiment, we use a Hubbard correction with a parameter U =3.5 eV. Anomalies in the acoustic branches of the phonon dispersion of ZrN and HfN, manifested as dips in the bands, can be understood through the nesting of Fermi surface determined from our calculations. To connect with transport properties, we have

---

The content of this chapter has been published as "*Electronic structure, phonons, and thermal properties of ScN, ZrN, and HfN: A first-principles study" Bivas Saha, Jagaran Acharya, Timothy D. Sands and Umesh V. Waghmare, Journal of Applied Physics, 033715,* ***107****, 2010.*

determined effective masses of ScN and determined their dependence on the *U* parameter. Using the relaxation time approximation in the Boltzmann transport theory, we estimate the temperature dependence of the lattice thermal conductivity and discuss the chemical trends among these nitrides. Our work uncovers important aspects of these nitrides for their potential applications in thermoelectric and thermionic devices.

2.1 Introduction

The early transition metal mononitrides are well known for their outstanding physical properties including high hardness, mechanical strength, high melting points, and electrical conductivity that vary from metallic to semiconducting. Because of these interesting features they have attracted wide attention of researchers and are extensively used in technological applications such as hard wear-resistant coatings, diffusion barriers, and optical coatings. Recently, these materials are also being investigated to understand their potential for thermoelectric applications.[1,2] As the growing demand for alternative clean energy catalyzes research in the thermoelectric field, we believe these materials ScN, ZrN, and HfN may have an important role to play in future thermoelectric devices, particularly at high operating temperatures where the refractory properties of the nitrides are a distinct advantage.

Electronic structures and vibrational spectra of these materials have been topics of research[5,6,9,10] for a considerable period of time. While most of these studies were aimed at understanding their physical properties, thorough analysis with a goal of assessing their potential for thermoelectric applications is much needed. The electronic structure of ScN has been intriguing as different groups have estimated different values of the band gap ranging from the zero band gap semimetallic[3,4] state to an indirect band gap semiconductor.[5,6] Recent experiments of Gall *et al.*,[7] however, suggests an indirect Γ to X gap of 0.9 ± 0.1 eV. Most recent theoretical work by Abdallah *et al.*,[8] based on the sophisticated *GW* approximation, has shown the same gap to be 0.99 ± 0.15 eV. Similarly, vibrational spectra of these materials have been calculated by Isaev *et al*[9] and Heid *et al.*[10] Interesting phonon anomalies in the acoustic branch of ZrN and HfN are well captured in their studies, and it would be nice to understand possible reasons for such phonon behaviour. To develop thermoelectric superlattices based on these nitrides, it is desirable to have a detailed comparative study of their electronic and thermal properties, which are relevant to thermoelectric behaviour.

Here, we use first-principles simulations to determine electronic structures, vibrational spectra, and thermal properties of ScN, ZrN, and HfN in the rock salt structure aiming to understand (a) their miscibility, and the feasibility of growing metal/semiconductor superlattices and heterostructures, (b) the detailed nature of their electronic structures, and (c) their vibrational spectra and thermal properties, for the potential applications in thermoelectric and thermionic devices. Our first-principles based DFT calculations should be useful to experimentalists in understanding properties of superlattices and multilayers of nitride materials relevant to thermoelectric applications.

2.2 Computational Details

We use plane wave self-consistent field (PWSCF) implementation of density functional theory (DFT), with a generalized gradient approximation (GGA)[11,12] to exchange correlation energy and ultrasoft pseudopotential[13] to represent the interaction between ionic cores and valance electrons. PWs with a cutoff energy of 30 Ry were used to represent the electronic wave functions and PWs with energy of 180 Ry were included for the description of charge density. Integration over the Brillouin zone is carried out using the Monkhorst–Pack scheme[14] with a 10x10x10 mesh of *k*-points, and occupation numbers are treated according to the Methfessel–Paxton[15] scheme with a broadening of 0.003 Ry. A Hubbard *U* correction[25] was included along with GGA in determination of the electronic structure of ScN. Lattice-dynamical calculations (the phonon spectrum, the density of states) are performed within the framework of the self-consistent density functional perturbation theory.[16] PWs with cutoff energies of 40 and 750 Ry were used to describe wave functions and charge density, respectively. Such a high charge density cutoff is necessary to keep the errors in vibrational frequencies minimal. In order to understand the detailed features of the phonon spectra, force constants (K) are obtained on a 4x4x4 *q*-point mesh. The dynamical matrices at arbitrary wave vectors were obtained using Fourier transform based interpolations.

The specific heat C_P and thermal conductivity $\kappa_{\alpha\beta}$ (i.e along any arbitrary $\alpha\beta$ direction) are given by Eqs. (1) and (2), respectively

$$C_P = \frac{1}{N_d}\sum_{\lambda q}\left[K_B\left(\frac{\hbar\omega_{\lambda q}}{K_B T}\right)^2\right]\frac{e^{\frac{\hbar\omega_{\lambda q}}{K_B T}}}{(e^{\frac{\hbar\omega_{\lambda q}}{K_B T}}-1)^2} \qquad (1)$$

$$\kappa = \hbar\sum_{\lambda}\int\frac{d^3q}{(2\pi)^3}\, v_{z\lambda}(q)^2\omega_{\lambda}\ (q)\tau_{\lambda}(\mathrm{q})(\frac{dn_B[\omega_{\lambda}(q)]}{dT}) \qquad (2)$$

where λ is the polarization vector of the normal mode, $v_{\alpha\lambda}(q)$ and $v_{\beta\lambda}(q)$ are the velocity of phonon along any α and β directions, respectively, $\tau_{\lambda}(q)$ is the relaxation time, and $n_B[\omega_{\lambda}(q)]$ is the boson occupation function. The relaxation time $\tau_{\lambda}(q)$ is assumed to be constant and kept outside the integral. Eigen frequencies were obtained in a dense mesh of 1000 *k*-points over the entire Brillouin zone, which are subsequently used in determining derivatives of phonon frequencies.

To get an idea about diffusion of cations across an interface in a superlattice, we determine energy of mixing for $Zr_xSc_{1-x}N$, $Sc_xZr_{1-x}N$, $Hf_xSc_{1-x}N$, and $Sc_xHf_{1-x}N$ with x =0.06 by considering configurations with 2x2x2 cubic supercell. There are total of 496 configurations, however analysis with site occupancy disorder technique[28] yields only five symmetry inequivalent configurations. The structures are relaxed until forces on each atom are less than 0.001 Ry/bohr, and the energy of mixing is calculated using the formula

$$E_{\text{mis}} = (E_{AmBnNm+n} - mE_{\text{AN}} - nE_{\text{BN}})/\,(m + n),$$

Where A and B represent transition metals, and E_{AN} is the energy of a nitride AN per formula unit, $E_{AmBnNmn}$ is the energy of alloy composed of m formula units of AN and n formula units of BN.

2.3 Results

2.3.1 Crystal structure

The three early transition mononitrides occur in rock salt crystal structure. Our estimates of the lattice constant and bulk moduli are compared with experimental and other theoretical values (see Table I). Our calculated values of bulk moduli are overestimated by a few to 10 % with respect to earlier GGA calculations,[5,9] but they are closer to the experimental values of ZrN and HfN.[17] For ScN, though our result is overestimated with respect to the experimental value,[18] it is within the typical GGA error and consistent with other calculations.

Energy of mixing of all configurations are very similar (see Table II) and negative, suggesting that diffusion of transition metal atoms into nitrides at the ZrN/ScN and HfN/ScN interface is quite possible and that the superlattice interface would not be atomically sharp. Our results suggest that Zr and Hf are more likely to diffuse to ScN side than Sc diffusing to ZrN or HfN.

TABLE I. Calculated lattice constant a (Å) and bulk modulus (B) of ScN, ZrN, and HfN are presented. Results of other calculations and values of experimental data are listed on the next line after results of our calculations.

System	a (Å)	B (Mbar)
ScN	4.52 4.50,[a] 4.51,[b] 4.50,[e] 4.44[f]	2.07 2.01,[a] 1.98,[b] 1.82±0.40[d]
ZrN	4.59 4.57,[a] 4.583,[b] 4.537,[g] 4.61[f]	2.89 2.64,[a] 2.50,[b] 2.85[c]

HfN	4.52 4.54,[a] 4.54,[b] 4.52[g]	2.94 2.78,[a] 2.69,[b] 3.03[c]

[a] Reference 5.

[b] Reference 9.

[c] Reference 17.

[d] Reference 18.

[e] References 19–21.

[f] Reference 22.

[g] Reference 23.

2.3.2 Electronic structure

As mentioned earlier, both experimental and theoretical estimates of the electronic band gap of ScN (see Table III) have been multivalued and contradicting. Freeman *et al.*[5] used screened-exchange local-density approximation (LDA) and derived an indirect Γ to X band gap of 1.58 eV, while Gall *et al.*[24] used DFT and the exact exchange formalism to predict an indirect band gap of 1.6 eV. Their experimental measurement[24] shows a band gap of 1.3±0.3 eV, with errors

TABLE II. Calculated energies of cation mixing in eV per formula unit. X =0.06 and the SICs represent different symmetry inequivalent configurations.

Multiplicity	$E_{Zr_xSc_{1-x}N}$	$E_{Sc_xZr_{1-x}N}$	$E_{Hf_xSc_{1-x}N}$	$E_{Sc_xHf_{1-x}N}$
SIC1	-0.0516	-0.0201	-0.0706	-0.0278
SIC2	-0.0529	-0.0197	-0.0729	-0.0280
SIC3	-0.0535	-0.0198	-0.0743	-0.0272
SIC4	-0.0518	-0.0191	-0.0715	-0.0273
SIC5	-0.0533	-0.0202	-0.0738	-0.0280

arising mainly from a large background carrier concentration causing an apparent increase in band gap. The most recent experiment of Gall *et al.*[7] suggests a band gap of 0.9±0.1 eV. In this work, we have used GGA coupled with a Hubbard U parameter[25] to fit the band gaps at different locations of the dispersion spectra. Our U=0.0 eV calculation shows that within GGA, ScN is semi-metallic in nature as found earlier by Srivastava *et al*.[26]. But such a discrepancy is not surprising as DFT is known to underestimate the band gap. It can be seen that for U =3.5 eV, we get an indirect Γ to X gap of 0.89 eV, direct Γ point gap of 2.93 eV, and X point gap of 1.86 eV, values that are reasonably close to experimental observations and other theoretical predictions. Although the direct gap at the Γ point is underestimated with respect to other DFT based calculations, the value is only slightly higher than experimental data. The gap at the X point, on the other hand is in better agreement with previous work.

TABLE III. Calculated band gaps of ScN, followed by other theoretical calculations and experimental observations.

Approach	**$E_{\Gamma\text{-}X}$ (eV)**	**E_X (eV)**	**E_Γ (eV)**
Present GGA+U	0.89	1.86	2.93
LDA + correction[25]	0.90	2.00	4.30
Screened exchange LDA[4]	1.58	2.41	4.80
$(G0W_0)_{\text{average}}$[5]	0.99	2.02	3.62
Experimental[22]	1.30±0.30	3.80	2.40
Experimental[5]	0.90±0.10		2.15

Calculated band structures of ScN (with a Hubbard U correction of U=3.5 eV), ZrN and HfN along high symmetry directions of the Brillouin zone (see Fig. 1(a)–1(c)) indicate that ZrN and HfN have similar band structures and both are metallic in nature with bands crossing the Fermi energy near the Γ, W and K points. Since both Zr and Hf are in the same column of the periodic table, and have the same oxidation state in their respective mononitrides with roughly the same lattice constants, such similarity in electronic structures is not surprising. Bandwidths in HfN are slightly larger than ZrN indicating larger coupling for HfN between *p*-states of nitrogen and *d*-states of the transition metals, consistent with its larger size. For ScN, semiconducting character is prominent in the band structure with a Γ to X (100 direction in Brillouin zone) band gap of 0.89 eV.

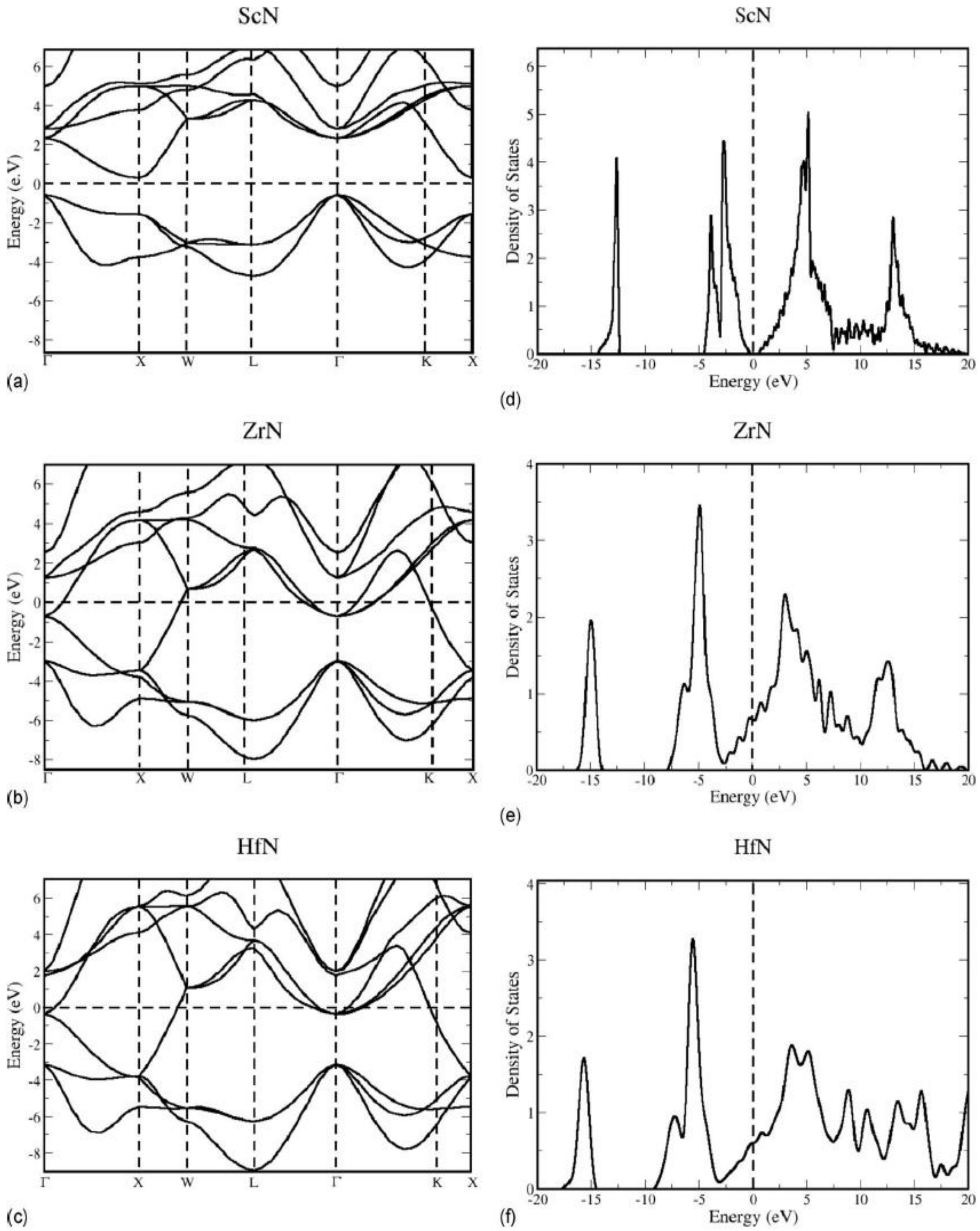

Figure 1. Electronic structure of (a) ScN, (b) ZrN, and (c) HfN, respectively, along high symmetry directions in the Brillouin zone. The symmetry points are Γ (000), X (010), W ($\frac{1}{2}$10), L (111), K ($\frac{3}{4}\frac{3}{4}$ 0) in the Brillouin zone, and density of electronic states of (d) ScN, (e) ZrN, and (f) HfN. A small gap in the spectrum of ScN and small asymmetry (linear behaviour) at E_F in the DOS of ZrN and HfN are evident.

The longitudinal (m_l) and transverse (m_t) effective masses of the conduction band at the X point in the band structure of ScN are calculated by fitting a quadratic function to the corresponding band energies along $\Delta(\Gamma{-}X)$ and $Z(X-W)$ directions, respectively, and for different values of U [see Table IV]. Monotonic increases in effective masses with varying U parameter are observed. Typically, the *d*-band width decreases with increasing U parameter (bands become more flat) resulting in the increase in effective mass found here. Our estimated effective masses are overestimated with respect to Abdallah *et al*.[8] G_0W_0 calculations (see Table IV). At present we are aware of only one experimental study where a conduction band effective mass between 0.1 and 0.2 has been reported (see Ref. 27).

The density of states (see Figs. 1(d)–1(f)) shows that the metal *d*-band $t_{2g}{}^3$ and $e_g{}^2$ states are split up in all three cases. The effect of splitting is most pronounced in the case of ScN, the peaks of $t_{2g}{}^3$ and $e_g{}^2$ states are separated by 8 eV. These peaks in ZrN are separated by 9.5 eV, and the splitting in HfN is slightly weaker. Another notable feature of the density of states (DOS) is that the 2*s*-bands of nitrogen in ZrN are shifted by 2.5 eV with respect to those in ScN and this shift is 2.8 eV in HfN. This should be relevant to estimation of valence band offsets in metal/semiconductor superlattices based on these nitrides.

To determine the nature of electronic states in valence and conduction bands, we visualize the electronic wave functions of the highest occupied (valence band) and lowest unoccupied (conduction) states at Γ point (see Fig. 2). The valence bands of ScN comprise primarily of the *p*-states of nitrogen and the lowest conduction bands are made of *xy*-type (t_{2g}) orbitals of Sc, as expected in octahedral coordination. For ZrN and HfN, both valence and conduction bands (which overlaps with each other) are based on mostly *d*-states of the transition metal (see these states of ZrN in Fig. 2). The overlap with *p*-states of nitrogen is reflected in the deviation in the shape of these states (see Fig. 2) from that of purely *d*-states.

TABLE IV. Calculated band gaps (in eV) and transverse (m_t*) and longitudinal (m_l*) effective masses of the conduction electron at the X point (in units of *m*0) with different *U* values for ScN.

Lower part of the table shows effective masses as reported in Ref. 8. at the same point of band structure. OEPx(cLDA) is an exchange correlation functional used by them.

U(eV)	**$E_{\Gamma\text{-}X}$**	**E_{Γ}**	**E_X**	**m_t^***	**m_l^***
0.0	0.008	2.42	0.93	0.164	1.571
1.0	0.270	2.56	1.21	0.197	1.718
2.0	0.496	2.69	1.45	0.228	1.840
3.0	0.748	2.84	1.72	0.262	1.981
3.5	0.890	2.93	1.86	0.281	2.061
4.0	1.031	3.02	2.01	0.301	2.175
5.0	1.350	3.22	2.34	0.344	2.378
Reference 8.					
OEPx(cLDA)-G_0W_0				0.189	1.483
OEPx(cLDA)				0.253	1.450
GGA				0.139	1.625

Fermi surfaces of ZrN and HfN consist of three branches (see results for ZrN in Fig. 3, those for HfN are very similar). The branch with the largest area (see Fig. 3(a)) represents a band crossing the Fermi energy near the W and K points of the Brillouin zone (see the electronic band structure Fig. (1). The other two branches of the Fermi surface (see Figs. 3(b) and 3(c)) are smaller, and correspond to the two bands that are crossing the Fermi energy near the Γ point. We will find the features of the Fermi surface presented here useful in understanding the phonon anomalies in sec. III C.

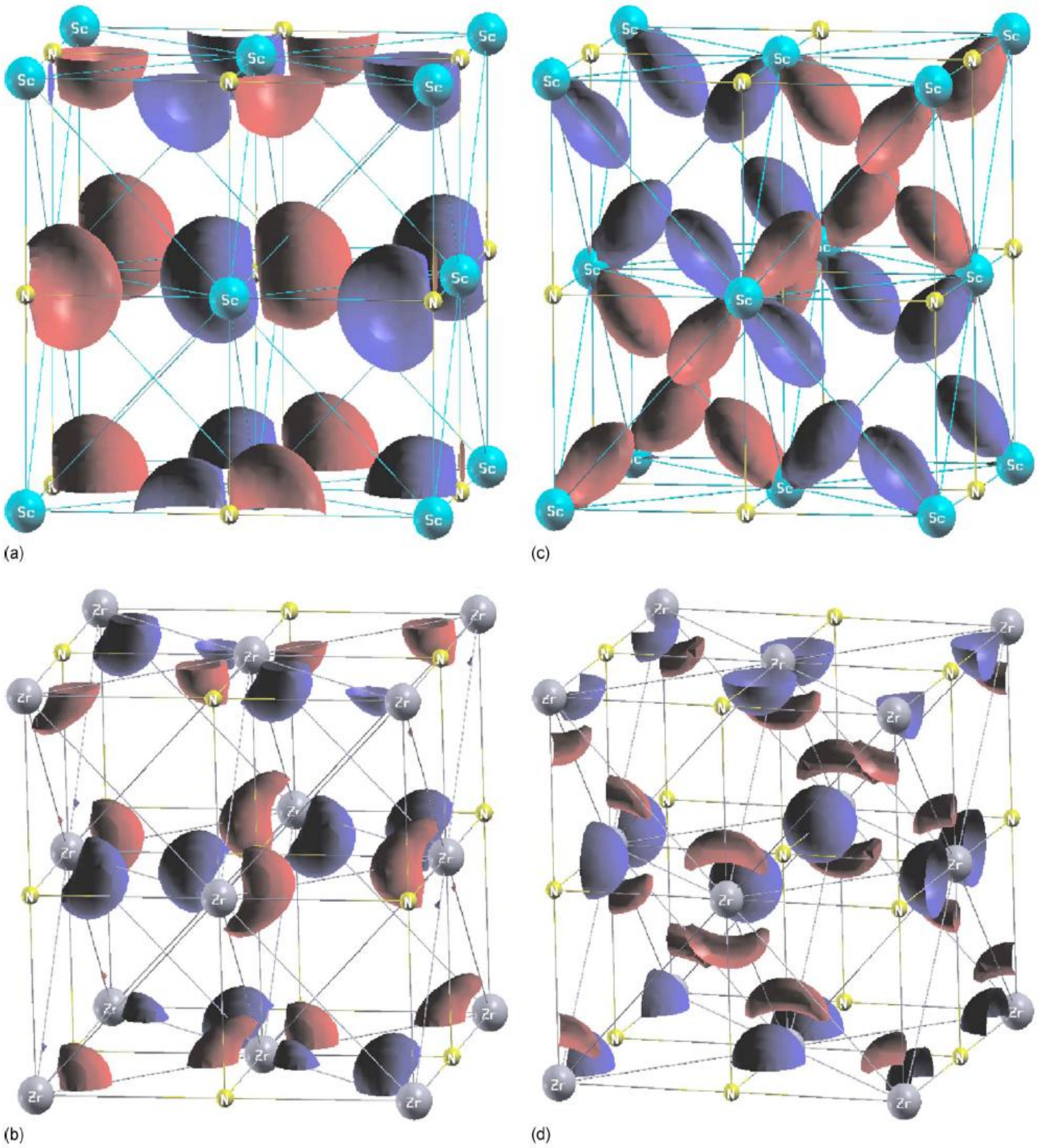

Figure 2. Nature of electronic states (at the Γ point) of the highest occupied valence band of (a) ScN and (b) ZrN, and lowest unoccupied conduction band (at the Γ point) for (c) ScN and (d) ZrN.

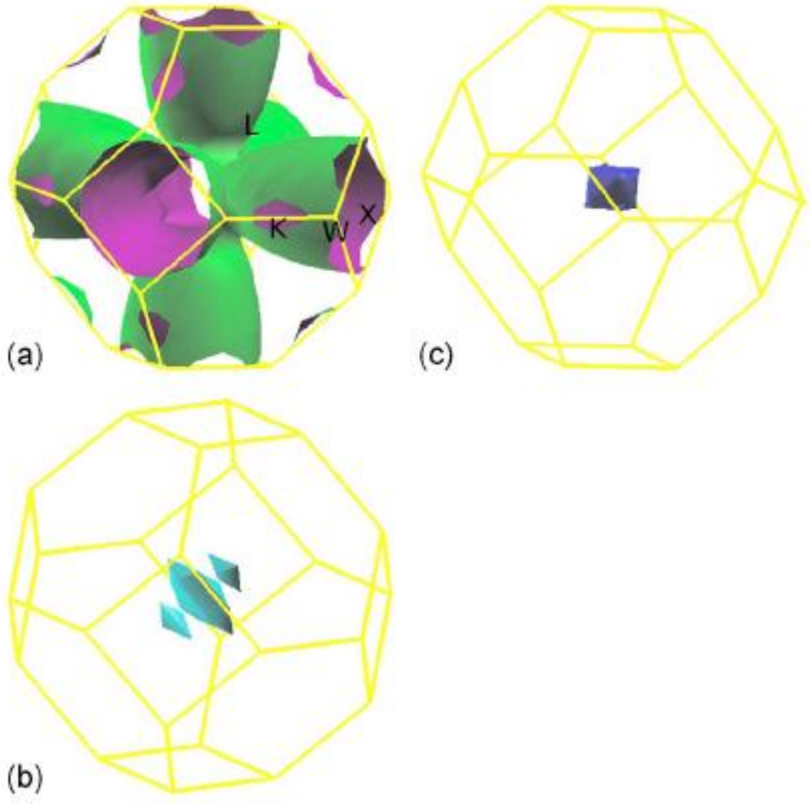

Figure 3. Different branches of Fermi surfaces of ZrN.

2.3.4 Phonons

A characteristic feature of the phonon dispersion of ScN (see Fig. 4) is the splitting of the longitudinal optical (LO) and transverse optical (TO) modes at the Γ point, which arises from long-range dipole-dipole interactions and is typical of polar semiconductors and insulators. Our estimates of the electronic dielectric constant $\varepsilon(\infty)$ and Born effective charge of ScN are 12.9 and 4.35, respectively, giving an LO-TO splitting of $\text{LO-TO}=335\text{cm}^{-1}$. The electronic dielectric constant, typically overestimated in DFT calculations, is quite comparable to that of other semiconductors like Si and GaAs. Our estimate of $\omega_{LO}{}^{2}/\omega_{TO}{}^{2}$ at the Γ point is about 5, which agrees well with Isaev *et al.*[9] estimation. Measured phonon dispersion curve of ScN is not available in the literature for comparison.

The branches of acoustic phonons of ScN are similar (albeit of slightly smaller slope) to those in rock salt oxides; they mix with optical phonons, but do not exhibit any anomaly. In contrast, there is an anomalous dip in the longitudinal acoustic modes of ZrN and HfN along the [100] (i.e. Γ to X direction near q=0.7), and both the longitudinal and transverse acoustic modes along the [110] (i.e., Γ to K to X) direction. Softening of these longitudinal and transverse acoustic modes can also be observed in [111] direction (i.e., Γ to L). Phonon dispersion curves also exhibit a reverse order in LO and TO modes along [100] direction nearly at (q =0.7). Such anomalies in phonon frequencies can be understood with the nesting of the Fermi surface by the wave vector (q). Due to large mass difference between nitrogen and transition metal Zr and Hf atoms, there are large gaps between the acoustic branches dominated by displacements of the heavy transition metals and optical modes involving displacements of mainly nitrogen atoms. The effect is less pronounced of ScN, where such gaps in the dispersion are not observed.

While our calculated dispersion for HfN is in good agreement with experimental observations (see Ref. 26), our calculated frequencies of optical modes in ZrN differ with respect to experimental observations (see Ref. 27), in which softer frequencies are reported at the Γ point, and a much higher frequency is observed at the X point of the Brillouin zone. The observed (Ref. 27) frequency of the optical phonon at the Γ point of ZrN is 468 cm^{-1}, whereas our estimate of the same is 490 cm^{-1}. Other optical frequencies are approximately 5%–8% softer than experimental estimates. However, our calculated phonon dispersion compares quite well with calculations of Isaev *et al.*[9] and Heid *et al.*[10]

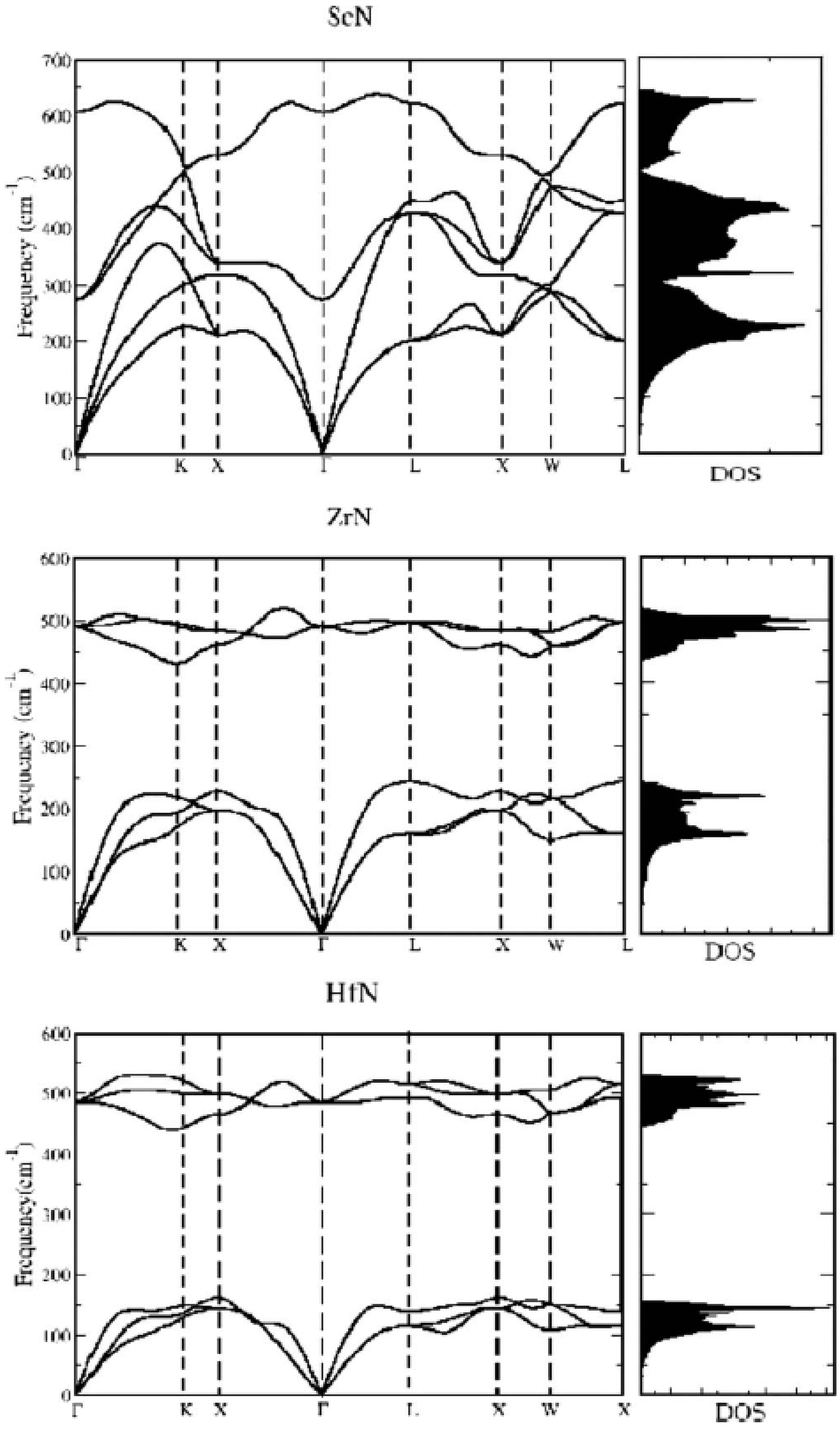

Figure 4. Calculated phonon dispersion curve and density of states of ScN, ZrN, and HfN in rocksalt structure. First columns has the phonon dispersion curves, while the right column has phonon DOS with same frequency scale. Gaps in the phonon spectra of ZrN and HfN are evident.

2.3.4 Thermal properties

Since the applications of these nitrides are expanding to thermoelectrics, we present a comparative theoretical analysis of thermal properties like specific heat and lattice thermal conductivity aiming to understand (a) the temperature dependence of the specific heat and lattice thermal conductivity and (b) the contribution of various phonon modes to thermal properties that will be useful in developing statistical thermo-dynamical model to predict thermal properties of their superlattices.

Our results for specific heats as a function of temperature (see Fig. 5) show that (below 300 K) HfN has the largest *Cp* followed by ZrN and ScN at low temperatures. This can be understood from the phonon dispersions presented earlier, acoustic branches (velocity of sound) of HfN are softer than those in ZrN and ScN. This is not surprising as these are dominated by Hf displacements and Hf has a larger mass compared to Zr and Sc. Since the specific heat at low temperature is dominated by acoustic phonons and is inversely proportional to the cube of the velocity of sound, the specific heat of HfN is the largest at low temperatures.

At high temperatures, the *Cp* values of all the three materials are identical to the Dulong Petit value (for diatomic system). A crossover to this classical limit is set by the effective Debye temperature. An estimate of Debye temperature (T_D) obtained using the slope of acoustic branches in our phonon dispersion; and an effective wave vector cut off are about 711, 512, and 326 K for ScN, ZrN, and HfN, respectively. We note that the specific heat of HfN remains higher than that of ScN and ZrN at all temperatures.

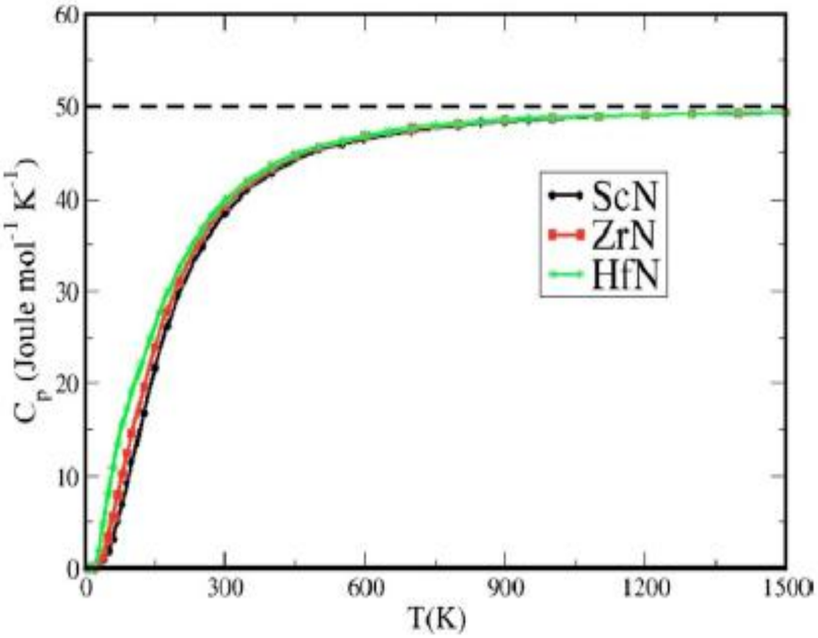

Figure 5. Lattice specific heat as a function of temperature of the three nitrides. Horizontal line represents classical Dulong–Petit limit of *Cp*.

We now analyze the lattice thermal conductivity using Boltzmann transport theory. Since we have not determined anharmonic interactions between phonons, it is not possible to estimate scattering time. We assume that the scattering time is constant for all phonons and compare the thermal conductivities of the three nitrides, including only the effects of DOS and group velocity of phonons. Our results for temperature dependent lattice thermal conductivity (see Figs. 6 and 7) show that κ of ScN is larger than the other two nitrides above 30 K. Since ScN is semiconducting in nature, the estimated *Cp* and κ_p should be roughly equal to the total

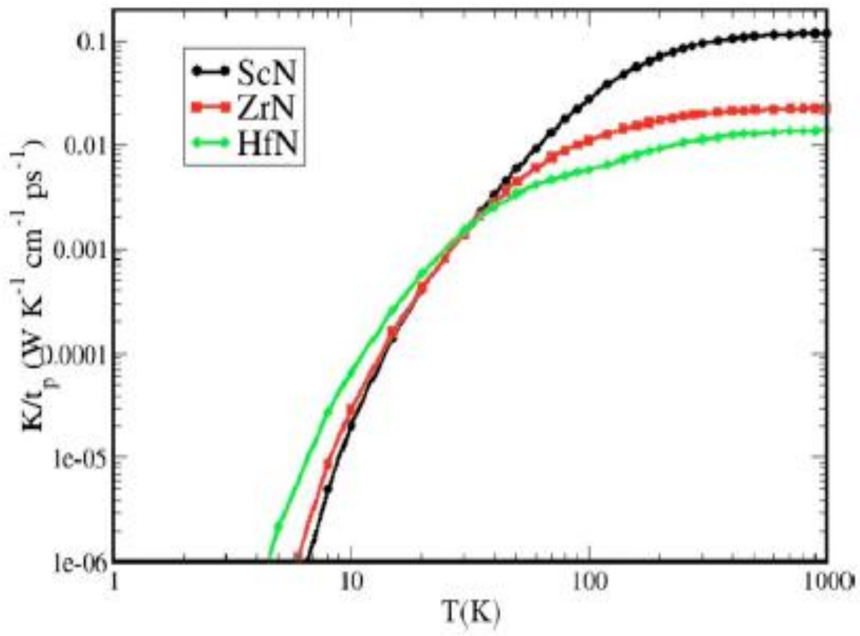

Figure 6. Estimated lattice thermal conductivity as a function of temperature of ScN, ZrN, and HfN.

values as the electronic contribution will be very small. It is clear from the phonon density of states (see Fig. 4) that a large number of phonons (both acoustic and optical phonons) of ScN fall in the mid-frequency range [250–500 cm^{-1}]. As a result, its lattice thermal conductivity is much higher than that of ZrN and HfN, where a large gap in the energies of acoustic and optical phonons is observed. While the gap between acoustic and optical modes is 191 cm^{-1} for ZrN, it is 283 cm^{-1} for HfN, and a cross over among thermal conductivities is observed at about 30 K below, which HfN has the largest thermal conductivity dominated by its acoustic phonons.

2.4 Potential for thermoelectric applications

Having discussed the physical properties of these nitrides in previous sections, we now comment on their potential use in making superlattices for thermoelectric applications. First of all, closely matched lattice constants (nearly perfect matching in the case of ScN and HfN, and ~1.5% lattice mismatch between ScN and ZrN) augur well for growing multilayers and superlattices, although one should be careful in analyzing their interfaces as the negative energy of miscibility suggests a tendency for diffusion of cations across the interface, potentially leading to diffuse interfaces at the atomic scale. Second, from our results for their electronic properties, these materials seem ideal for growing metal/semiconductor (ZrN/ScN and HfN/ScN) superlattices, with a moderate band gap of ScN that can be utilized for controlling the Schottky barrier height, a key parameter for the energy filtering mechanism that can be used to tune the Seebeck coefficient and optimize the power factor.[1,29] Third, the proposed nitride metal/semiconductor superlattices should also act as phonon filters for reduction of lattice thermal conductivity, due to large gap in the phonon spectra of ZrN and HfN, mismatching with a high density of phonons of ScN in the same range of energy. We predict that HfN/ScN superlattices should have smaller lattice thermal conductivity compared to ScN/ZrN as the extent of the gap between acoustic and optical phonons is larger for HfN than ZrN. Surely; more work on superlattices of these nitrides is desirable to assess their effectiveness for thermoelectric applications. Our results here should form a starting point for development of models and further analysis of superlattices.

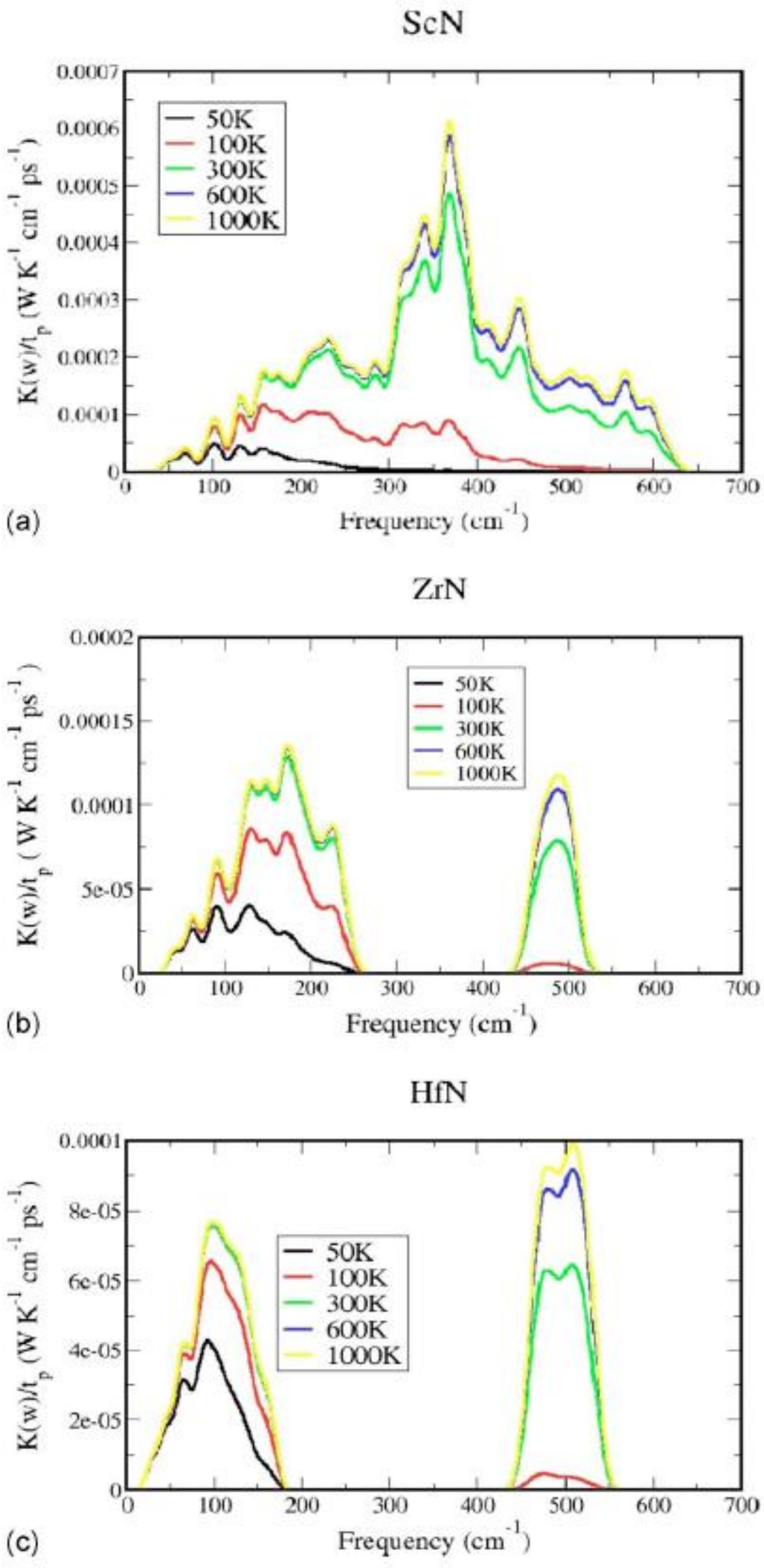

Figure 7. Phonon contribution to thermal conductivity of (a) ScN, (b) ZrN, and (c) HfN, at various temperatures, as a function of phonon frequencies.

2.5 Conclusions

In conclusion, we have presented a comparative first-principles theoretical analysis of electronic structure, vibrational spectra and thermal properties of bulk ScN, ZrN, and HfN, with a motivation to assess their potential for thermoelectric applications. While ScN is a semiconductor with a small electronic band gap, ZrN and HfN are metals exhibiting a large gap in their phonon spectra. Thus, metal/semiconductor superlattices based on these nitrides can act as filters for both electrical charge and phonon thermal transport, with implications for enhancement in their thermoelectric properties. While typical DFT calculations fail to capture the semiconducting electronic gap of ScN, we demonstrate that inclusion of a relatively cost-effective Hubbard *U*-correction with an appropriate choice of U=3.5 eV can be used to obtain a reasonable description of the electronic structure of ScN. Anomalies in the phonon dispersion of metallic ZrN and HfN, manifested as dips in acoustic branches, can be understood through the nesting of the Fermi surface as determined from our calculations. To connect with transport properties, we have determined electronic effective masses of the conduction band in ScN and used Boltzmann transport theory to estimate the temperature dependence of the lattice thermal conductivity. Analysis of the temperature dependence and chemical trends in thermal transport properties of these nitrides should be useful in further work on nanoscale superlattices of these nitrides with enhanced thermoelectric properties.

References

1. M. Zebarjadi, Z. Bian, R. Singh, A. Shakourie, R. Wortman, V. Rawat, and T. Sands, J. Electron. Mater., 960, **38 (**2009).

2. V. Rawat, Y. Koh, D. Cahill, and T. Sands, J. Appl. Phys., 024909, **105** (2009).

3. G. Travaglini, F. Marabelli, R. Monnier, E. Kaldis, and P. Wachter, Phys. Rev. B, 3876, **34** (1986).

4. R. Monnier, J. Rhyner, T. M. Rice, and D. D. Koelling, Phys. Rev. B, 5554, **31** (1985).

5. C. Stampfl, W. Mannstadt, R. Asahi, and A. J. Freeman, Phys. Rev. B, 155106, **63 (**2001).

6. W. R. L. Lambrecht, Phys. Rev. B, 13538, **62** (2000).

7. H. A. Al-Brithen, A. Smith, and D. Gall, Phys. Rev. B, 045303, **70** (2004).

8. A. Qteish, P. Rinke, M. Scheffler, and J. Neugebauer, Phys. Rev. B, 245208, **74** (2006).

9. E. I. Isaev,S. I. Simak, I. A. Abrikosov, R. Ahuja, Y. K. Vekilov, M. I. Katsnelson, A. I. Lichtenstein, and B. Johansson, J. Appl. Phys., 123519, **101 (**2007).

10. R. Heid, K.-P. Bohnen, B. Renker, T. Wolf, and H. Schober, Phys. Rev. B, 092302, **71 (**2005).

11. J. P. Perdew, K. Burke, and M. Ernzerhof, Phys. Rev. Lett., 3865, **77** (1996).

12. X. Hua, X. Chen, and W. A. Goddard III, Phys. Rev. B , 16103, **55** (1997).

13. D. Vanderbilt, Phys. Rev. B, 7892, **41** (1990).

14. H. J. Monkhorst and J. D. Pack, Phys. Rev. B, 5188, **13** (1976).

15. M. Methfessel and A. Paxton, Phys. Rev. B, 3616, **40** (1989).

16. S. Baroni S. de Gironcoli, A. D. Corso, P. Giannozzi, Rev. Mod. Phys. 515, **73** (2001).

17. X.-J. Chen, V. V. Struzhkin, Z. Wu, M. Somayazulu, J. Qian, S. Kung, A. N. Christensen, Y. Zhao, R. E. Cohen, H.-K. Mao, and R. J. Hemley, Proc. Natl. Acad. Sci. U.S.A., 3198, **102** (2005).

18. D. Gall, I. Petrov, N. Hellgren, L. Haltman, J. E. Sundgren, and J. E. Green, J. Appl. Phys., 6034, **84** (1998).

19. W. Lengauer, J. Solid State Chem., 412, **76 (**1988).

20. V. A. Gubanov, Z. W. Lu, B. M. Llein, and C. Y. Fong, Phys. Rev. B, 4377 , **53** (1996).

21. K. T. Park, K. Terakura, and N. Hamada, J. Phys. C, 1241, **20** (1987).

22. R. W. G. Wyckoff, *Crystal Structure*, 2nd ed. (Wiley, New York, 1963), Vol. 1, p. 86.

23. *Structure Reports*, edited by W. B. Pearson (International Union of Crystallography, Utrecht, 1993).

24. D. Gall, M. Stadele, K. Jarrendahl, I. Petrov, P. Desjardins, R. T. Haasch, T.-Y. Lee, and J. E. Greene, Phys. Rev. B, 125119, **63** (2001).

25. V. I. Anisimov and O. Gunnarson, Phys. Rev. B, 7570, **43** (1991).

26. S. Duman, S. Bagci, H. M. Tutuncu, G. Ugur, and G. P. Srivastava, Diamond Relat. Mater.. 1175, **15** (2006).

27. G. Harbeke, E. Meier, and J. P. Dismukes, Opt. Commun., 335, **4** (1972).

28. R. Grau-Crespo, S. Hamad, C. R. A. Catlow, and N. H. de Leeuw, J. Phys.: Condens. Matter., 256201, **19** (2007).

29. D. Vashaee and A. Shakouri, Phys. Rev. Lett., 106103, **92** (2004).

Chapter 3

Electronic structure, vibrational spectrum and thermal properties of YN: A first-principles study

Abstract

YN is a promising semiconductor for use in metal/semiconductor superlattices for thermoelectric applications. We present first-principles density functional theory based simulations to determine its electronic structure, vibrational spectra and thermal properties using a generalised gradient approximation of the exchange correlation energy. We employ a combination of GGA+U and GW approximation based techniques to (a) correctly estimate the band gaps and (b) determine specific features of its electronic structure relevant to transport properties, such as transverse (m_t^*) and longitudinal (m_l^*) conduction band effective mass. With a motivation of forming alloys of YN with other materials, we have determined the volume deformation potentials. Our results for phonons show, a large longitudinal optical (LO) and transverse optical (TO) splitting at the Γ point of the vibrational spectrum with a gap of 325 cm^{-1} arising due to long-range dipole-dipole interactions. An estimate of lattice specific heat and Boltzmann transport theory based calculations of lattice thermal conductivity and its variations with temperature are included to assess YN's potential for thermoelectric applications.

The content of this chapter will be submitted for publication soon.

3.1 Introduction

Early transition nitride materials are very hard, chemically stable and possess high corrosion resistance. They are also interesting from the fundamental point of view due to their unusual and diverse properties. They have a wide range of applications from cutting tools, protective coatings to hard coating for magnetic storage devices. Recently, a lot of research efforts are being invested in understanding their potential for energy and environment related applications.

YN crystallizes in the rocksalt structure and is a promising material for thermoelectric and thermionic applications. It is of current interest and is being studied experimentally to tune thermal properties through the formation of alloys with other nitride materials. Though there are first-principles based studies on the structure and the electronic properties of YN, the estimate of its band gap is multivalued and unclear. Moreover, the transport related properties like transverse and longitudinal band effective mass have not been estimated yet. It is also necessary to enumerate its different volume deformation potentials.

We note a very nice work of Isaev et al[3], where they determined vibrational spectra of YN. Here we benchmark our work through comparison with theirs, and take it forward to estimate thermal properties such as lattice specific heat and lattice thermal conductivity, and compare it with that of ScN and rationalize its suitability for technological applications.

DFT calculations based on LDA & GGA are well known for underestimation of band gaps of semiconductors or insulators. In particular for transition nitride materials, their performance is even poor. Both in the case of YN and ScN, standard GGA based calculations show semi-metallic or semiconducting nature with the Γ-X band gap of 0.2-0.3 eV[1,14]. Several techniques have been developed over the years to correct this band gap problem of DFT, with examples like screened-exchange LDA[2], (LDA,GGA)+U[4], GW[4,15] approximation and others. While (LDA,GGA)+U technique takes into account the on-site Hubbard interaction correction, GW approximation works by taking into account the self energy correction and is by far the most reliable technique to correctly estimate band gaps of semiconductors. Rather than solving the Kohn-Sham equations, one solves the Dyson equations in GW approach taking into account the self energy corrections, although self-consistency in GW is still a matter of debate and tends to produce higher estimates of band gap.

Here in this work, we present a combination of GGA+U and GW approach to correctly estimate the band gaps, volume deformation potential and transverse and longitudinal conduction band effective mass. A GGA method is used to correctly estimate the vibrational spectra, lattice specific heat, lattice thermal conductivity and it’s variation with temperature to understand YN’s suitability and potential for thermoelectric applications.

3.2 Methods of calculation

We use PWSCF implementation of density functional theory (DFT), with a generalized gradient approximation (GGA)[6,7] to exchange correlation energy and ultrasoft pseudopotential[8] to represent the interaction between ionic cores and valence electrons. Plane wave basis set (PWs) with an energy cut-off energy of 30 Ry was used to represent the electronic wave functions and PWs with an energy cutoff 180 Ry were included for the representation of charge density. Integration over the Brillouin zone is carried out using the Monkhorst-Pack[9] scheme with a 10x10x10 mesh of k-points and occupation numbers are smeared according to the Methfessel-Paxton[10] scheme with a broadening of 0.003 Ry. Hubbard U corrections was included along with GGA in determination of the electronic structure of YN.

Lattice -dynamical calculations (the phonon spectrum, the density of states) are performed within the framework of the self consistent density functional perturbation theory[11]. Plane waves with cut off energy 40 Ry and 750 Ry were used to describe wave functions and charge density respectively. Such high energy cutoffs are necessary to keep the errors in vibrational frequencies of nitrides minimal[12]. Integration over the Brillouin zone is performed using 18 x 18 x 18 mesh of k-points. In order to understand detailed feature of phonon spectra, force constant (K) are obtained on a 4 x 4 x

4 q-point mesh. The dynamical matrices at arbitrary wave vectors were obtained using Fourier transform based interpolations of force constant matrices.

The specific heat Cp and thermal conductivity κ are given by

$$C_p = \frac{1}{N_q}\sum_{\lambda \mathrm{q}}[\mathrm{k_B}\,(\frac{\hbar\omega_{\lambda \mathrm{q}}}{\mathrm{k_B T}})^2\;\frac{\mathrm{e}^{\frac{\hbar\omega_{\lambda \mathrm{q}}}{\mathrm{k_B T}}}}{(\mathrm{e}^{\frac{\hbar\omega_{\lambda \mathrm{q}}}{\mathrm{k_B T}}}-1)^2}] \qquad 1$$

$$\kappa_{\alpha\beta} = \hbar\sum_{\lambda}\int\frac{d^3q}{(2\pi)^3}v_{\alpha\lambda}(q)v_{\beta\lambda}(q)\omega_{\lambda}(q)\tau_{\lambda}(q)\left[\frac{dn_B\,[\omega_{\lambda}(q)\,]}{dT}\right] \qquad 2$$

where $v_{\beta\lambda}(q)$ is the velocity of the phonon, $\tau_{\lambda}(q\;)$ is the relaxation time, and $n_B\,[\omega_{\lambda}(q)]$ is the Bose-Einstein distribution function. The relaxation time $\tau_{\lambda}(q)$ is assumed to be constant and taken outside the integral. Eigen frequencies are obtained in a dense mesh of k-points over the entire Brillouin zone, which are subsequently used in determining $v_{\alpha\lambda}(q)$ using finite difference formula.

GW calculations are done using the VASP package[16] of the density functional theory, with PAW-GGA potentials to represent the interaction between ionic cores and valence electrons. Integration over the Brillouin zone is performed using 8 x 8 x 8 mesh of k-points and energy cutoff of 400 eV was used to represent the interaction between ionic cores and valence electrons. The GW self-energy operator Σ = iGW, where G is the Greens function and W is the screened Coulomb interaction, is constructed using the GGA results.

3.3 Results

3.3.1 Crystal Structure

Like most of the early transition nitride materials, YN crystallises in rocksalt structure under ambient conditions. Our estimates of lattice constant and bulk modulus (see Table I) are within typical DFT errors of experimental measurement. Our estimates of lattice constant with PWSCF based GGA calculation yields slightly better accuracy than VASP based PAW-GGA calculations. Bulk modulus is in reasonable agreement with both the methods employed, and also compares well with an all-electron theoretical investigation[2] giving us confidence in our calculation details.

Table I: Calculated lattice constant a (Å) and bulk modulus (B) of YN. Results of our calculations are presented in first two rows, followed by literature values.

Methodology	a (Å)	B (GPa)
GGA	4.90	160
PAW-GGA	4.93	163
FLAPW-GGA[2]	4.85	163
Expt.[13]	4.87	-----

3.3.2 Electronic structure

To determine the electronic structure of YN relevant to thermoelectric applications, we have estimated direct and indirect band-gaps with GGA and GGA+U calculations, and projector augmented wave basis set for GW approximation calculations. Though there are certain first principles based reports on the band-gap of YN, there has been no consensus on its electronic structure. Our DFT calculations within GGA show that YN is an indirect band-gap semiconductor with the indirect Γ-X band gap of 0.21 eV, and direct gaps at the Γ and X point being 0.60 eV and 3.14 eV

TABLE II: Estimated direct and indirect band gaps at different regions of the dispersion spectrum using GGA coupled with a Hubbard U parameter, and increasing U values. m_l^* and m_t^* represents longitudinal and transverse conduction band effective mass at the X point of the dispersion spectrum.

U (eV)	$E_{\Gamma\text{-X}}$ (eV)	E_X (eV)	E_Γ (eV)	$m_l^*(m_0)$	$m_t^*\ (m_0)$
0.0	0.21	0.60	3.14	1.31	0.141
0.5	0.37	0.77	3.20	1.37	0.162
1.0	0.45	0.85	3.23	1.41	0.174
1.5	0.54	0.94	3.27	1.47	0.186
2.0	0.63	1.04	3.31	1.51	0.198

2.5	0.73	1.14	3.35	1.56	0.212
3.0	0.83	1.25	3.40	1.68	0.228
3.5	0.94	1.36	3.45	1.73	0.244
4.0	1.06	1.49	3.51	1.83	0.261
4.5	1.19	1.62	3.57	1.97	0.280

respectively. Similar result was also indicated by Mancera et al[1] using all electron based FP-LAPW calculations. Their results suggest an indirect Γ-X band gap of 0.31 eV, while direct gaps at the Γ and X point being 0.62 eV and 3.10 eV respectively. Screened exchange LDA calculation of Freeman et al[2] however suggested an indirect band gap of 0.85 eV. Using GGA coupled with a Hubbard U parameter, we estimate both the direct and indirect band-gaps of YN as a function of U parameter. Estimates of band-gap presented (see Table II); shows monotonic increase of the indirect and the direct band-gaps as a function of U parameter. The indirect Γ-X band gap of 0.83 eV, and direct gap at Γ and X point of 3.4 eV and 1.36 eV respectively, estimated with U=3.0 eV, are in good agreement with Freeman et al's [2]

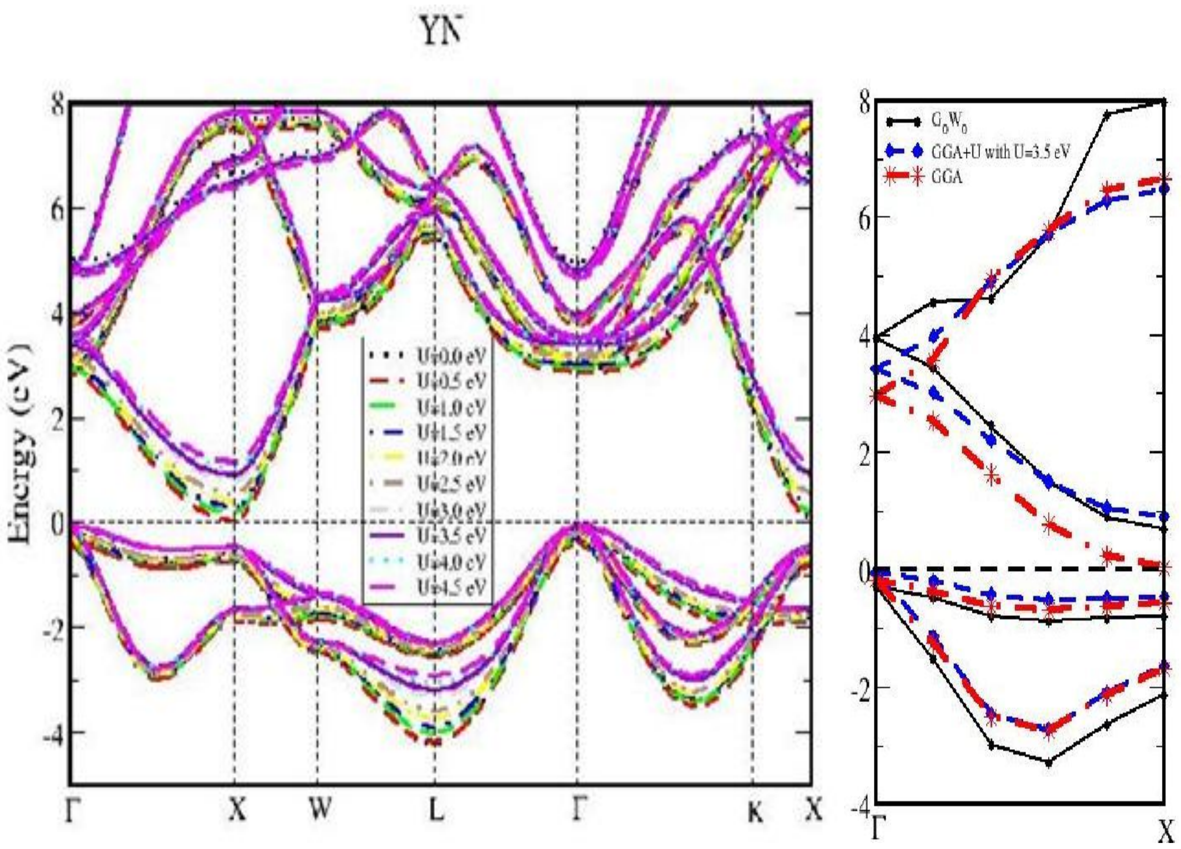

Figure 1 Electronic structure of YN calculated using GGA+U, and G_0W_0 approach. (a) The band diagram along the high symmetry directions of the Brillouin zone. (b) Comparison of the band diagram along Γ-X direction using GGA, GGA+U with U=3.5 eV, and G_0W_0 approach.

TABLE III: Calculated direct and indirect band-gaps of YN using GW approximation calculation with different self consistent steps.

No. of self consistent steps	$E_{\Gamma\text{-}X}$ (eV)	E_X (eV)	E_Γ (eV)
1st	0.97	1.46	4.20
2nd	1.14	1.66	4.50
3rd	1.20	1.72	4.58
4th	1.22	1.74	4.61

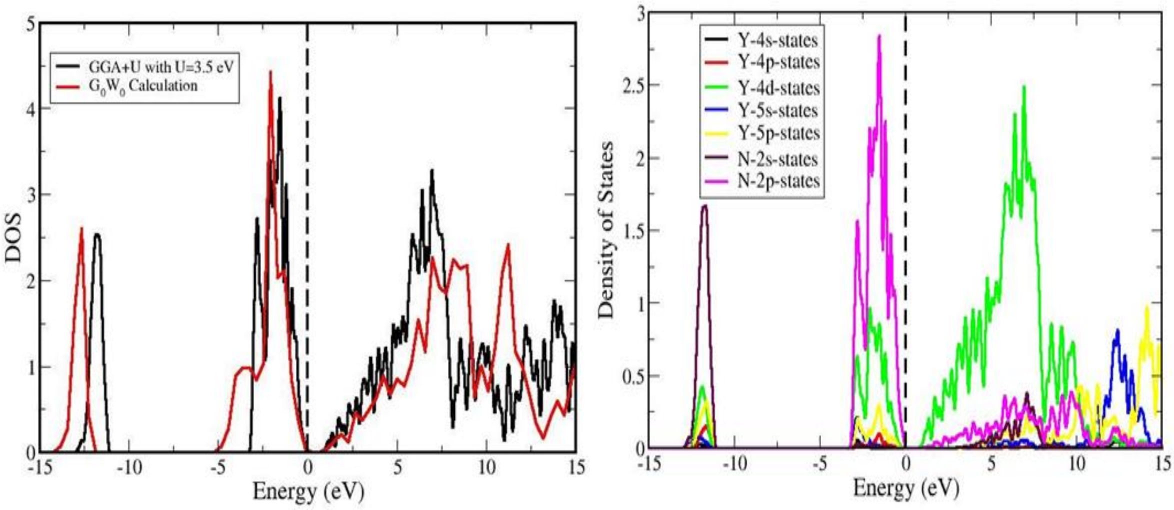

Figure 2 Electronic densities of states of YN. (a) The total densities of states calculated using the GGA+U method with U=3.5 eV, and G_0W_0 approximation. (b) The partial densities of states i.e. the contribution of different atomic orbital's on DOS of YN.

calculation. The values compare well with another theoretical calculation by Zerroug et al[17], where they have reported an indirect gap of 0.8 eV.

Our results with G_0W_0 approximation (see Table III) yield an indirect Γ-X band gap of 0.97 eV, and the direct gaps at Γ point of 4.2 eV and at the X point of 1.46 eV. As the number of self consistent step in the calculation is increased, the band gaps increases (see Table III), and ultimately converges by the 4th cycle. We have already pointed out that GW based estimations does over estimate the band gaps, and hence we will use only the results of zeroth order in the self-energy (G_0W_0) corrections in the rest of the work.

The estimated electronic structure of YN along the high symmetry directions of the Brillouin zone a function of Hubbard U parameter [see Fig 1.] shows an increase in the indirect Γ-X band gap with increasing U parameter. Direct gaps at the Γ and the X point of the dispersion spectrum also increase in the same manner. The dispersion resembles that of other transition nitride semiconductors like ScN[12] and LaN[2]. One obvious effect of Hubbard U parameter is that the band width of *4-d* Sc orbital becomes lesser with increasing U values. The dispersion

TABLE IV: Theoretical estimates of different band-gap volume deformation potential (a_v^{α}) (in eV) for YN using different methods.

Method Used	$a_v^{\Gamma-X}$	$a_v^{\Gamma-\Gamma}$	a_v^{X-X}
G_0W_0	2.07	1.41	2.79
GGA	1.68	1.57	2.47
GGA+U with U=3.5 eV	2.60	1.20	3.45

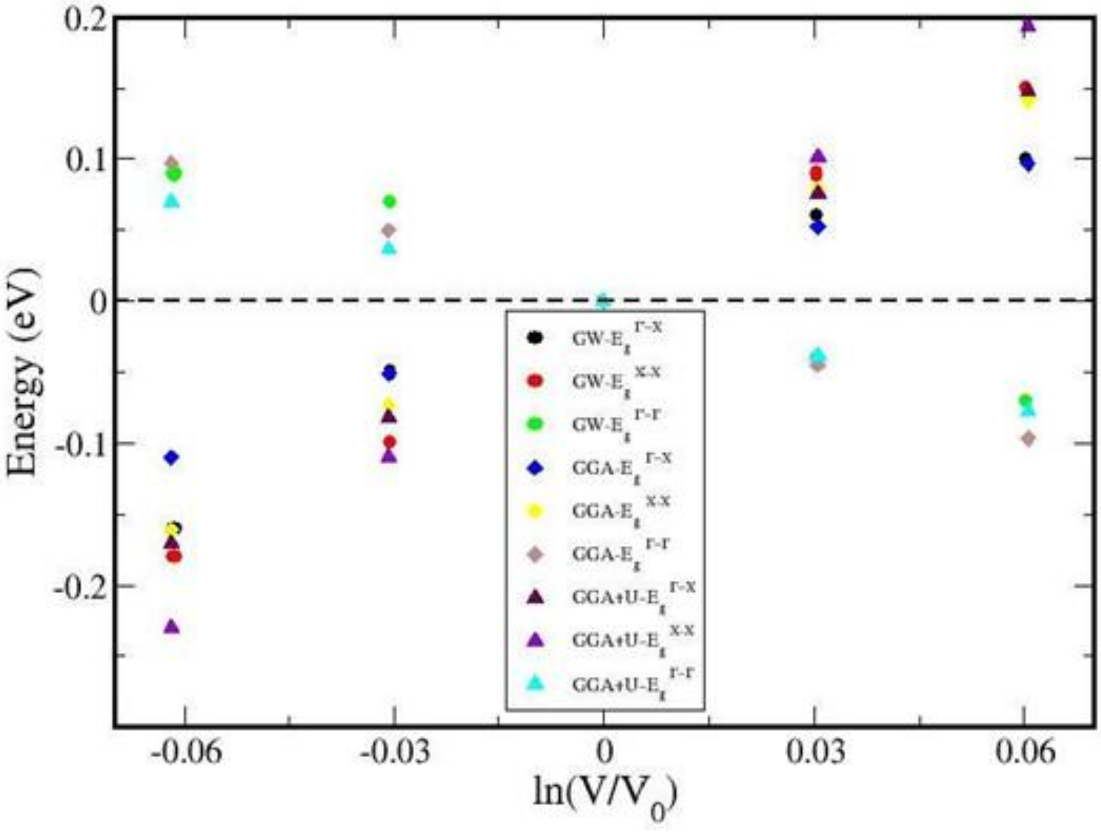

Figure 3 Changes in direct and indirect band gaps as a function of change in the volume of the unit cell, calculated using GGA, GGA+U, and G_0W_0 approach.

spectra along Γ-X direction (see Fig. 1) calculated using GGA, GGA+U with U=3.5 eV, and G_0W_0 approach compare well with each other, apart from the fact that introduction of Hubbard U parameter introduces a relatively larger gap along the Γ-X direction which was

absent in GGA calculation. The shapes of the valance and conduction bands estimated using G_0W_0 approach are in good agreement with GGA, and GGA+U calculations.

The total DOS (see Fig 2) calculated using GGA+U with U=3.5 eV, and G_0W_0 approach compare well with each other, albeit slight difference in the valance band N *s*-states. The valance band width of N *p*-states is relatively larger for G_0W_0 approach calculation compared to GGA+U method. The partial DOS [see Fig. 2] indicate strong hybridization between the transition element and nitrogen states, with the energy position and width of bands in the partial DOS for N and Y atoms appearing very similar.

To connect with the transport properties of YN relevant for thermoelectric applications, the longitudinal (m_l^*) and transverse (m_t^*) conduction band effective mass at the X point of the dispersion spectrum are calculated by fitting a quadratic function to the corresponding band energies along the (Γ-X) and the Z(X-W) directions respectively, and for different values of U parameters [see table II]. Monotonic increases in effective masses with increasing U parameter are observed consistent with reduction in the *d*-band width with increasing U parameter, (bands become more flat) resulting in the increase in effective mass found here. To the best of our knowledge the effective masses of YN has not been measured experimentally yet, neither there is any report of theoretical estimates of m_l^* and m_t^*.

With a motivation of forming alloys of YN with other nitrides, we have estimated the indirect and direct band-gaps as a function of its lattice constant using all the three approaches, namely G_0W_0 approximation, GGA and GGA+U with U=3.5 eV. Results indicate increase in indirect Γ-X band gap, as well as direct gap at the X point of the dispersion curve, and decrease in direct gap at the Γ point, as we increase the lattice constant from -2% to 2% with respect to the equilibrium values [see Fig 3]. The volume deformation potentials a_v^α for the band gaps $E_g^{\Gamma-X}$, $E_g^{\Gamma-\Gamma}$ and E_g^{X-X} are calculated using the formula $\frac{dE_g^\alpha}{dln\,(V/V_0)}$ [see ref 13],

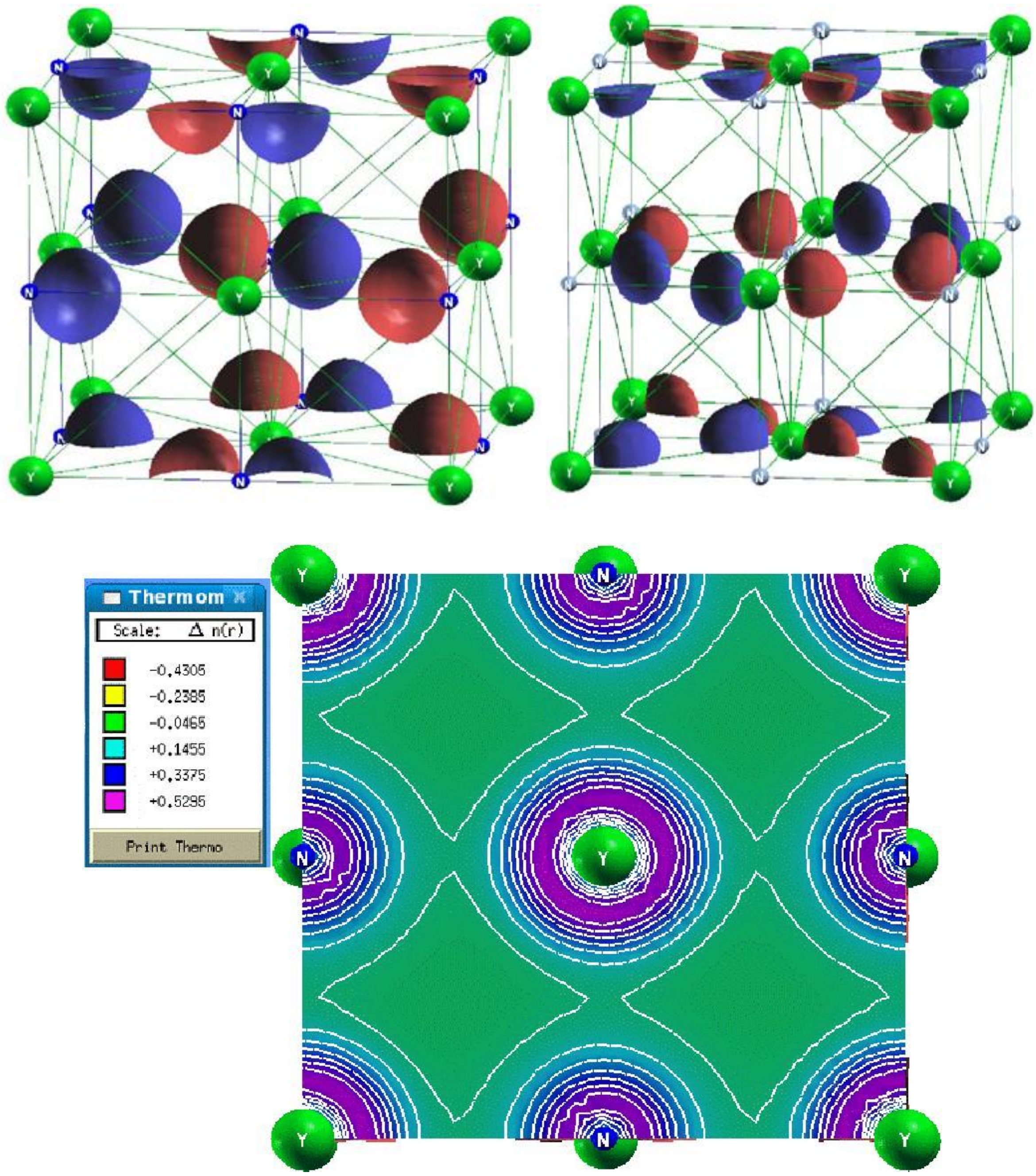

Figure 4 Nature of electronic states (at the Γ point) of (a) the highest occupied valance band, and (b) lowest unoccupied conduction band (at the Γ point). (c) Charge density in a YN plane.

where V_0 denotes the volume of the unit cell at equilibrium lattice constant and V is the volume at a lattice constant slightly displaced from equilibrium value (see estimates in Table IV). We find that the volume deformation potentials do have dependence on the methodology employed. To the best of our knowledge no theoretical or experimental reports on the volume deformation potentials of YN are available in literature. But the results compare well with that of ScN estimated by Qteish et al[18]. Their estimates of $E_g^{\Gamma-X}$, $E_g^{\Gamma-\Gamma}$ and E_g^{X-X} with OEPx(cLDA)-G_0W_0 are 2.02 eV, 1.54 eV, and

2.04 eV respectively, whereas our estimates of the same with G_0W_0 approach are 2.07 eV, 1.41 eV, and 2.79 respectively for YN.

To elucidate the nature of electronic states in valence and conduction bands, we visualize the electronic wave functions of the highest occupied (valence band) and lowest unoccupied (conduction) states at the Γ point (see Fig. 4), as well as charge density in an YN plane (see Fig. 5). The valence bands of YN comprise primarily of the *p*-states of nitrogen and the lowest conduction bands are made of xy - type (t^2g) orbital of Y, as expected in octahedral coordination.

3.3.3 Vibrational Spectra

Vibrational spectrum of YN is essential to understand its potential for technological applications, particularly for developing thermoelectric and thermionic based solid state energy conversion devices. The phonon dispersion curve of YN (see in Fig 5) resembles that of ScN, and is typical to those of rocksalt structured materials with no anomaly. Long range dipole-dipole interaction has resulted in splitting of the longitudinal optical (LO) and transverse optical (TO) modes at the Γ point of the dispersion curve. Our estimates of the electronic dielectric constant $\varepsilon(\infty)$ and Born effective charge of YN are 13.1 and 4.5

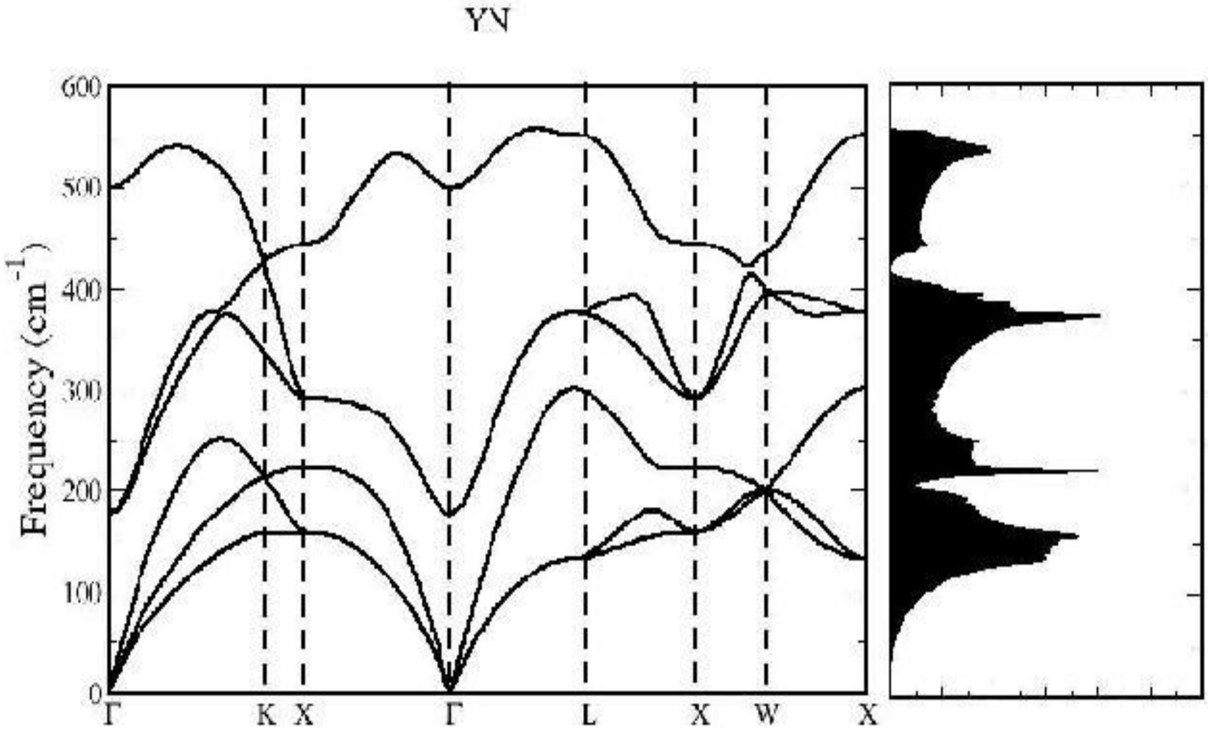

Figure 5. Calculated phonon dispersion curve and density of states of YN in rock salt structure. First columns has the phonon dispersion curves, while the right column has phonon DOS with same frequency scale.

respectively, giving an LO-TO splitting of 335 cm^{-1}. Our results of $\omega_{LO}^2 / \omega_{TO}^2$ at the Γ point is about 8.1, which is smaller than Isaev et al's[3] calculation of 10.1. The present estimation is also higher than that of ScN where a value of 5 is reported[12]. To the best of our knowledge no experimental phonon dispersion curve of YN is available.

Although there is a large difference between the masses of Y and N, the acoustic and optical modes of dispersion spectrum are not separated by a gap, unlike the transition metal nitride of Zr; situated in the same row of the periodic table. This is similar to the presence of no gap in ScN. The frequencies are however softer than ScN dispersion spectrum, owing to Y's larger mass than Sc.

3.3.4 Thermal Properties

Thermal properties of YN are of great interest to understand its technological applications. Here, we present theoretical estimates of lattice specific heat, lattice thermal conductivity and it's variation with temperature, to understand its suitability for thermoelectric applications. Our estimate of the specific heat as a function of temperature for YN is shown in Fig 5. The characteristic variation of Cp resembles with that of other transition nitride materials like ScN, ZrN, HfN and approaches classical Dulong Petit value at higher temperatures. The Debye temperature (T_D) is also estimated using the acoustic branches of the dispersion curve; and results show T_D is about 564 K for YN. The present estimation of T_D is a little lower than that of ScN, which had T_D about 711 K[12].

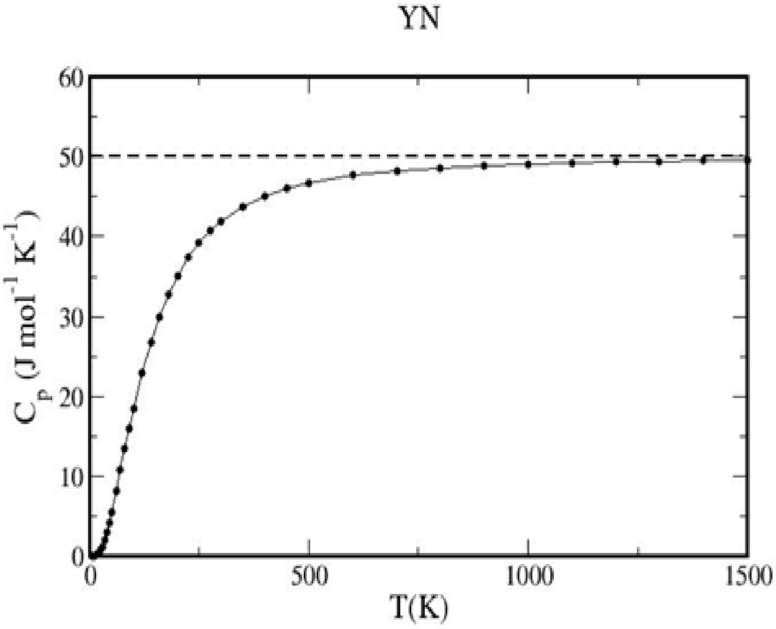

Figure 6. Lattice specific heat as a function of temperature of YN. Horizontal line represents classical Dulong–Petit limit of *Cp*.

We now analyze the lattice thermal conductivity using Boltzmann transport theory. Since, we have not determined anharmonic interactions between phonons, it is not possible to estimate scattering time. We assume that the scattering time is constant for all phonons and compare thermal conductivities of the three nitrides, which include only the effects of density of states

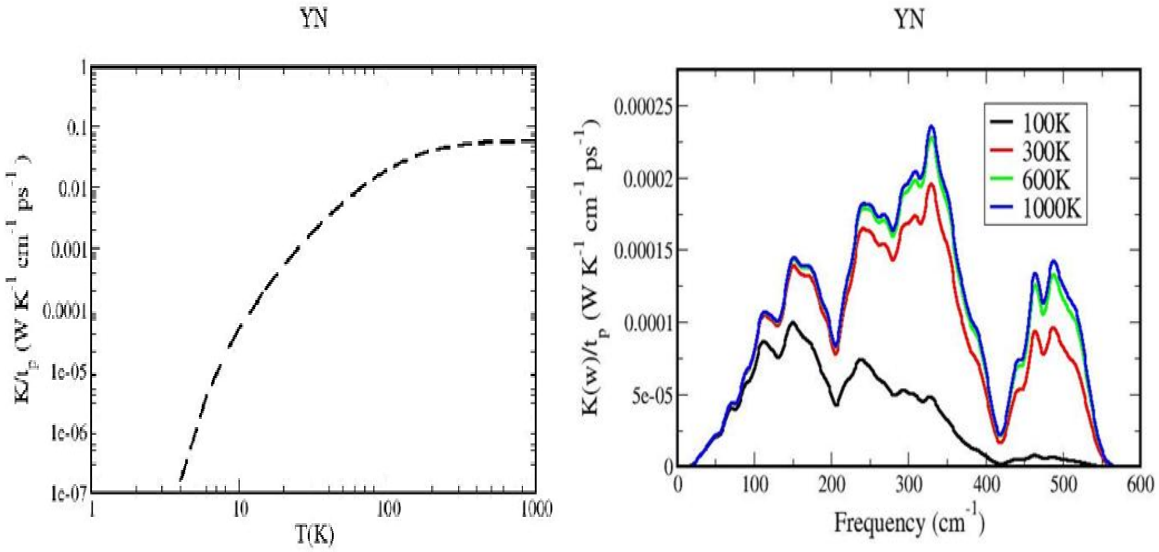

Figure 7. (a) Estimated lattice thermal conductivity as a function of temperature of YN. (b) Change in lattice thermal conductivity as a function of phonon frequencies.

and group velocity of phonons. Change in lattice thermal conductivity (see Fig. 7) as a function of temperature indicates convergence of κ at temperatures above 300 K. The contribution to lattice thermal conductivity as a function of phonon frequency [see Fig 7.] shows dominance of mid-frequency range [200-400 cm^{-1}] phonons in κ at high temperatures (above 100 K). At lower temperatures though, long wave-length acoustic phonons dominates in lattice thermal conductivity.

3.4 Conclusions

In conclusion, we have reported first-principles density functional theory based calculations of electronic structure, vibrational spectra and thermal properties of YN, with a motivation to understand its potential for thermoelectric applications. Our results suggest, YN is an indirect band-gap semiconductor with the Γ-X band gap of 0.97 eV, suitable for applications in metal/semiconductor superlattices. To connect with transport properties, longitudinal and transverse conduction band effective mass at the X point of the dispersion spectrum is estimated as a function of Hubbard U-parameter. Band-gaps volume deformation potentials are calculated to determine YN's relevance to use in alloys or superlattices. Phonon dispersion, phonon density states and thermal properties like lattice specific heat, lattice thermal conductivity (κ) and it's with temperatures is reported suggesting YN's suitability as semiconductor component in the metal/semiconductor based thermoelectric materials.

References

1. L. Mancera, J. A. Rodriguez and N. Takeuchi, J Phys. Condens. Matter., 2625, **15** (2003).

2. C.Sampfl, W. Mannstadt, R. Asahi, and A. J. Freeman, Phys. Rev. B, 155106, **63** (2001).

3. Isaev et al J. Appl. Phys., 123519, **101** (2007).

4. V. I. Anisimov and O. Gunnarson, Phys. Rev. B, 7570, **43** (1991).

5. M. L. Tiago, S. Ismail-Beigi and S. Louie; Phys. Rev. B, 125212, **69** (2004).

6. John P. Perdew, Kieron Burke, and Matthias Ernzerhof, Phys. Rev. Lett., 3865, **77** (1996).

7. Xinlei Hua, Xiaojie Chen, and W. A. Goddard III, Phys. Rev. B, 16103, **55** (1997).

8. D. Vanderbilt., Phys. Rev. B, 7892, **41** (1990).

9. H. J. Monkhorst and J. D. Pack, Phys. Rev. B, 5188, **13** (1976).

10. M. Methfessel and A. Paxton, Phys. Rev. B, 3616, **40** (1989).

11. S. Baroni, S.de Gironcoli, A. Dal. Corso, P. Giannozzi, Rev. Mod. Phys., 515, **73** (2000).

12. B, Saha, J. Acharya, T. Sands and U. V. Waghmare, Journal of Applied Physics, 033715, **107** (2010).

13. P. Villars and L. D. Calvert, Pearsons Handbook of Crystallographic Data for Intermetallic Phases American Society for Metals, Metals Park, Ohio, 1985.

14. S. Duman, S. Bagci, H. M. Tutuncu, G. Ugur, and G. P. Srivastava, Diamond Relat. Mater., 1175, **15** (2006).

15. M. Shishkin and G. Kresse, Phys. Rev. B, 235102, **75** (2007).

16. M. Shishkin and G. Kresse, Phys. Rev. B 035101, **74** (2006).

17. S. Zerroug, F. Ali Sahraoui, and N. Bouarissa, Applied Physics A, DOI 10.1007/s00339-009-5243-x.

18. A. Qteish, P. Rinke, M. Scheffler, J. Neugebauer, Phys. Rev. B, 245208, **74** (2006).

Chapter 4

Thermoelectric properties of ZrN/ScN and HfN/ScN metal/semiconductor superlattices

Abstract

We present first-principles density functional theory based simulations to determine electronic structures, vibrational spectra and thermal properties of ZrN/ScN and HfN/ScN metal/semiconductor superlattices and solid solutions aiming at (a) understanding the role of interfaces and epitaxial strain in controlling the transport of electrons and phonons, (b) developing models that can be employed in determination of such properties of these superlattices with periodicities longer than those of the short-period superlattices modelled here, for potential applications in the thermoelectric and thermionic solid state energy conversion. Our results show (a) large asymmetry of the electronic density of states and flattening of electronic bands along the cross-plane direction near the Fermi energy of these superlattices, (b) the presence of Schottky barriers essential for optimizing ZT in these material systems. Analysis of vibrational spectra and Boltzmann transport based calculations shows 10-100 fold reduction of lattice thermal conductivity along the growth direction of

---

A part of this chapter is submitted for publication. The other portion is under preparation.

these superlattices with respect to their individual bulk components due to phonon filtering at the interfaces resulting from the mismatch in bulk phonon density of states. HfN based superlattices have been proven to be better in reducing lattice thermal conductivity due to Hf's larger mass than Zr. Temperature dependence of lattice thermal conductivity also suggests significant contribution of optical phonons on lattice thermal conductivity at room temperature, with effect most pronounced in case of HfN based superlattices. Our work uncovers important features of metal/semiconductor superlattices necessary to understand their suitability for thermoelectric and thermionic applications.

4.1 Introduction

Thermoelectric materials that convert heat flux directly into electrical power have enormous promise in dealing with the challenges of the growing demand for alternative clean energy, and are a subject of great scientific interest[1-2]. These materials are characterised by a dimensionless figure of merit $ZT = \frac{S^2\sigma T}{\kappa}$, where S is the Seebeck coefficient, σ is the electrical conductivity, κ is the thermal conductivity and T is the absolute temperature. To be competitive with conventional refrigerators and power generators, we must develop materials with ZT=3 to 4. Research in the last few years with conventional bulk materials[3-4] has yielded ZT of about 1.0 to 1.5. Achieving ZT > 2 is challenging due to mutually conflicting design parameters (e.g. σ and κ) in ZT. Pioneering works of Dresselhaus et al[5-6] and subsequent experiments of Harman et al[7] and Venkatasubramanian et al[8] showed that nanostructured materials have the potential for higher ZT.

Multilayers and superlattices[9-12] grown by alternate deposition of metal and semiconductor materials with nanoscale periods are being explored as potential candidates with higher ZT. The central ideas are (1) to control the Schottky barrier height for efficient energy filtering of electrons during transport, thereby enhancing the Seebeck coefficient, while retaining a high electrical conductivity, and (2) to use the interface between the component materials as a phonon filter, thereby reducing the cross-plane lattice thermal conductivity. Understanding the nature of the metal/semiconductor interface[13] is crucial to designing multilayers or superlattices with high ZT.

In this chapter, we present first-principles density functional theory based simulations of electronic structure and vibrational spectra, as a foundation for developing an understanding the temperature-dependent cross-plane transport properties of two promising metal/semiconductor superlattices: ZrN/ScN and HfN/ScN. We note that ScN is semiconducting in nature with an indirect Γ-X band gap of 0.89 eV, while ZrN and HfN are metallic in nature. Their multilayers (superlattices) have been investigated experimentally in earlier work by Rawat et al[14].

4.2 Methods of calculation

We use the PWSCF implementation of the DFT with a generalised gradient approximation (GGA)[16] to the exchange correlation energy and ultrasoft pseudopotentials[17] to represent the interaction between ionic cores and valence electrons. Plane wave (PW) basis sets with energy cutoffs of 30 Ry and 180 Ry were used to represent the electronic wave function and charge density respectively. Integration over the Brillouin zone is carried out using the Monkhorst-Pack[18] scheme with a 10x10x10/n mesh of k-points for n/n superlattice, and occupation numbers are smeared using the Methfessel-Paxton[19] scheme with a broadening of 0.003 Ry. A Hubbard U correction[20], with U=3.5 eV was included along with GGA for Sc atoms to correctly describe the electronic bandwidth and gap. (See details and validity of our methods used in extensive analysis of bulk properties of ScN, ZrN and HfN in Ref. 15.)

Phonon spectra and density of states are determined accurately within the framework of self-consistent density functional perturbation theory[21], with plane wave basis of energy cutoffs of 40 Ry and 750 Ry to describe the wave function and charge density respectively. In order to understand the detailed features of phonon spectra, force constant matrices were obtained on a

3x3x1 [for 2/2superlattice] q-point mesh. The dynamical matrices at arbitrary wave vectors were then obtained through Fourier transform based interpolation.

The lattice thermal conductivity $\kappa_{\alpha\beta}$ (i.e along αβ direction) is obtained within Boltzmann theory

$$\kappa_{\alpha\beta} = \hbar \sum_{\lambda} \int \frac{d^3q}{(2\pi)^3} v_{\alpha\lambda}(q) v_{\beta\lambda}(q) \omega_{\lambda}(q) \tau_{\lambda}(q) \left\lfloor \frac{dn_B\,[\omega_{\lambda}(q)]}{dT} \right\rfloor \qquad (1)$$

Where λ is the polarization vector of the normal mode, $v_{\alpha\lambda}(q)$ and $v_{\beta\lambda}(q)$ are the group velocities of the phonon along α and β directions respectively, $\tau_{\lambda}(q)$ is the relaxation time, and $n_B\,[\omega_{\lambda}(q)]$ is the Bose-Einstein distribution function. The relaxation time $\tau_{\lambda}(q)$ is assumed to be constant and kept outside the integral. Eigen frequencies were obtained on a dense mesh of 1000 k-points over the entire Brillouin zone, which were subsequently used in determination of $v_{\alpha\lambda}(q)$ and $v_{\beta\lambda}(q)$.

The lattice specific heat is also given by the following expression

$$C_P = \frac{1}{N_d} \sum_{\lambda q} \left[K_B \left(\frac{\hbar\omega_{\lambda q}}{K_B T} \right)^2 \right] \frac{e^{\frac{\hbar\omega_{\lambda q}}{K_B T}}}{\left(e^{\frac{\hbar\omega_{\lambda q}}{K_B T}} - 1\right)^2} \qquad (2)$$

4.3 Results

4.3.1 Crystal Structure

Since the individual bulk nitride materials satisfy (a) similarity in crystal structure, (b) nearly equal lattice constants and other criterion for growing them epitaxially, they are perfectly suited to form superlattices and multilayers. In our computational study we have generated superlattice structures by periodically stacking m layers of metals, and n layers of semiconductors. Both the in-plane and cross-plane lattice constant is optimized, and structures are relaxed until force on each atom is less than 0.001 Ry/Bohr.

The in-plane lattice constant for ZrN/ScN superlattice is 4.55 Å (Note the lattice constant of ZrN and ScN are 4.59 Å, and 4.52 Å respectively), and for HfN/ScN superlattice it is 4.52 Å (the lattice constant of HfN is 4.52 Å). One key aspect of our calculation is that the interfaces in all the superlattices are perfectly epitaxial. Given below are some schematic diagrams of the superlattice under study.

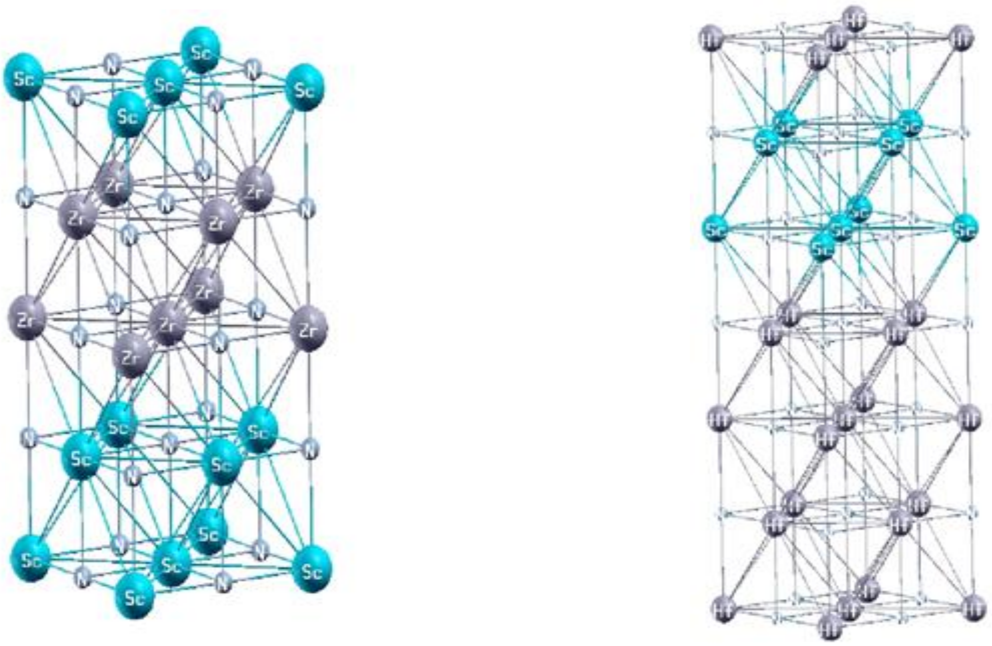

2/2 ZrN/ScN superlattice

4/2 HfN/ScN superlattice

Figure 1 Schematic diagram of 2/2 ZrN/ScN and 4/2 HfN/ScN metal/semiconductor superlattice.

The cross-plane lattice constant (c) increases linearly with the increase in the number of metal/semiconductor layers with fig (2) shows the linear behaviour. The 2/4 and 4/2 ZrN/ScN and HfN/ScN superlattices also have almost the same c value as that of 3/3 superlattices.

The interface energy density calculated using the formula

$$(E_{(\text{bulk-ScN})}+E_{(\text{bulk-MN})}-E_{(\text{ScN/MN})}) \tag{3}$$

signifies the preference of the individual bulk materials to form interface with other nitride materials. Fig 2 also indicates the convergence of interface energy as we increase the thickness of superlattices.

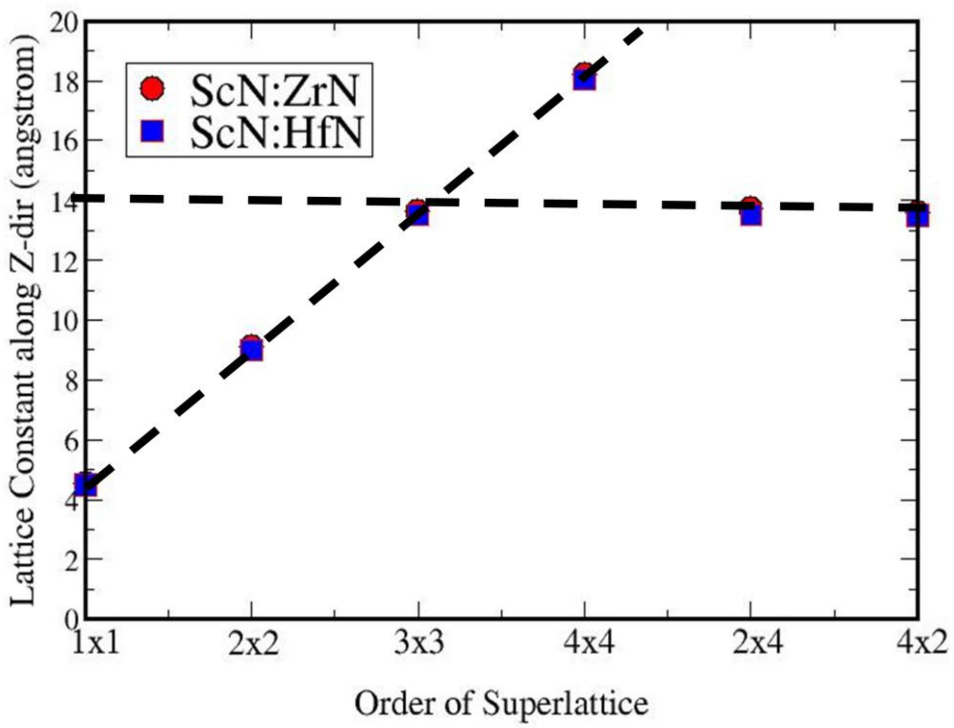

Figure 2 Cross-plane lattice constant (c) for various superlattices. Linear increase in c with increasing number of period thickness is observed.

Because of the perfect lattice constant matching between ScN and HfN, the interface energy density of HfN/ScN is higher relative to ZrN/ScN superlattices, where nearly 1.5% lattice mismatch between the components materials exist.

We have also estimated the inter-planer distances for all the superlattices, and results suggest epitaxial interface with almost the same inter planer distances between ScN and metal nitride for both the superlattice system under consideration.

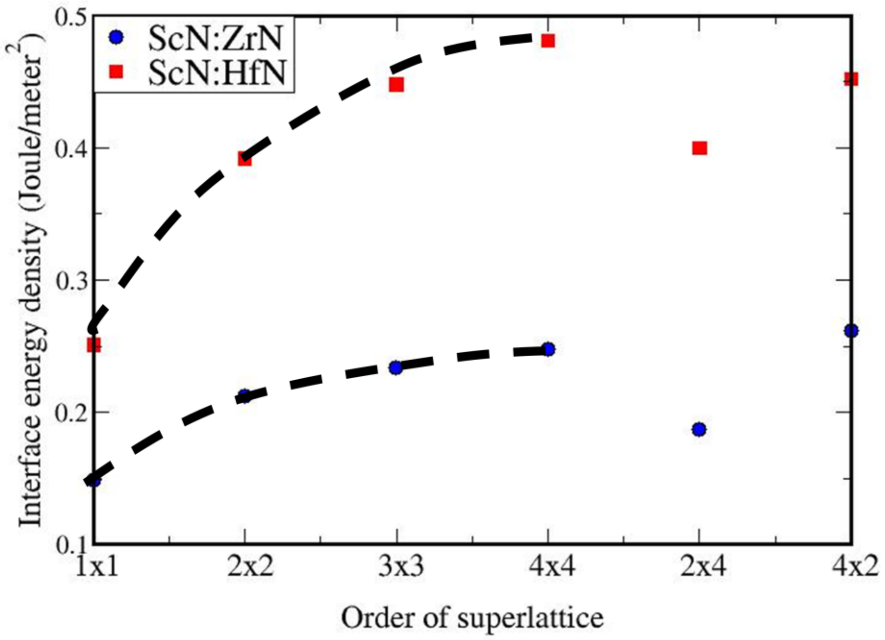

Figure 3. Interface energy density of superlattices calculated using the formula ($E_{(bulk-ScN)}+E_{(bulk-MN)}-E_{(ScN/MN)}$). Results suggest convergence to longer periodicity at 1.8 nm.

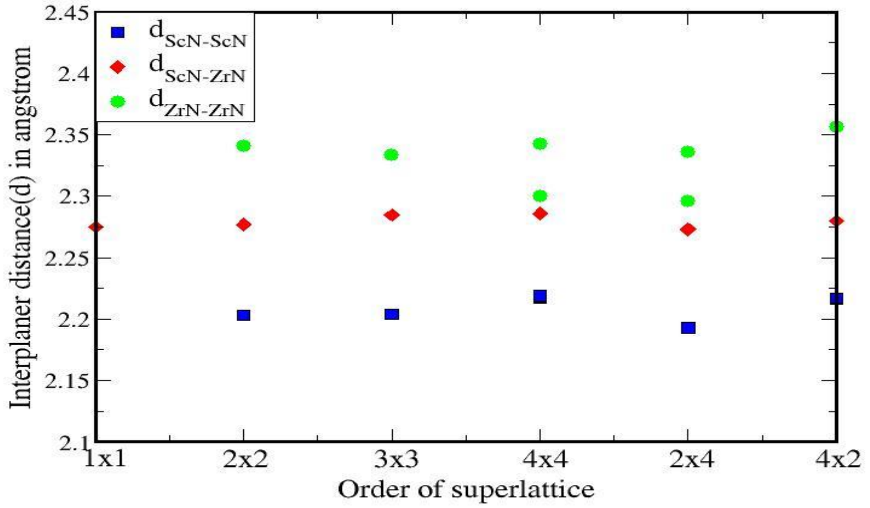

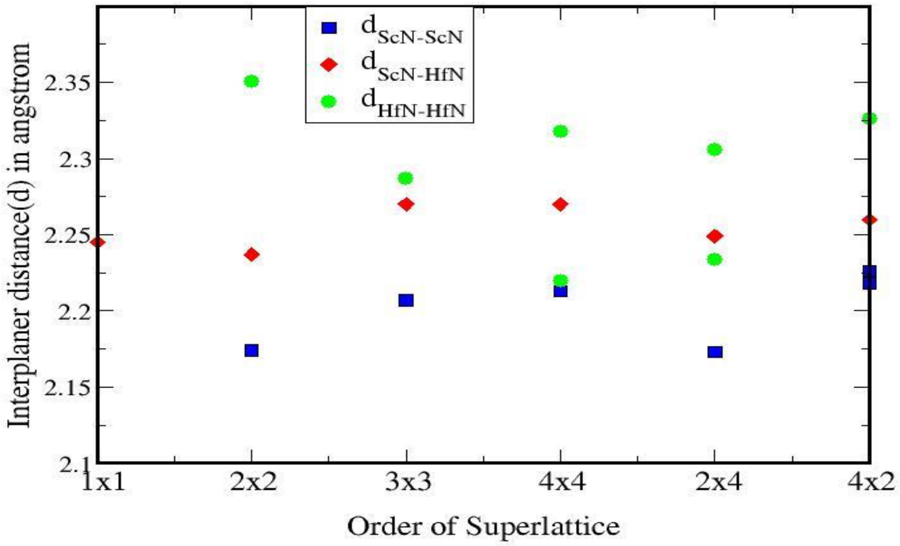

Figure 4 Inter planer distances of ZrN/ScN and HfN/ScN superlattices.

4.3.2 Electronic Structure

Electronic structure of these metal/semiconductor superlattices is intriguing for the enhancement of ZT. While we have determined the electronic structure of m/n metal/ScN superlattices with m & n = 1 to 4, here we present the results of 2/2 superlattices. The dispersion spectra [see Fig. 1(a)] show that the superlattices are metallic for the in-plane transport (i.e. Γ-X), while there are relatively flat bands (near the Fermi energy) along the cross-plane direction (i.e. Γ-Z). These nearly flat bands will increase the effective mass of electrons, thereby increasing the Seebeck coefficient along the cross-plane direction. The normalised density of states exhibits a large asymmetry at the Fermi energy [see Fig. 1(b)], (much higher density of states at $E \geq E_F$ than at $E \leq E_F$) which is necessary within the Mahan & Sofo[22] theory for large thermopower. Another notable feature of the DOS is that the ZrN (HfN) and ScN's *2s* valence band states of nitrogen are all aligned in the superlattices, while in bulk ZrN (HfN) they were shifted by 2.5 eV (2.8 eV) with respect to those in ScN. Thus these electronic superlattices should be effective in filtering out low energy electrons at the Schottky barriers, key to enhancement of the Seebeck coefficient as discussed by Shakouri et al[10].

From the dispersion curves it is also clear that these superlattices are highly degenerate along the cross-plane growth directions with the bottom of Γ-Z valance band lying just below the Fermi energy.

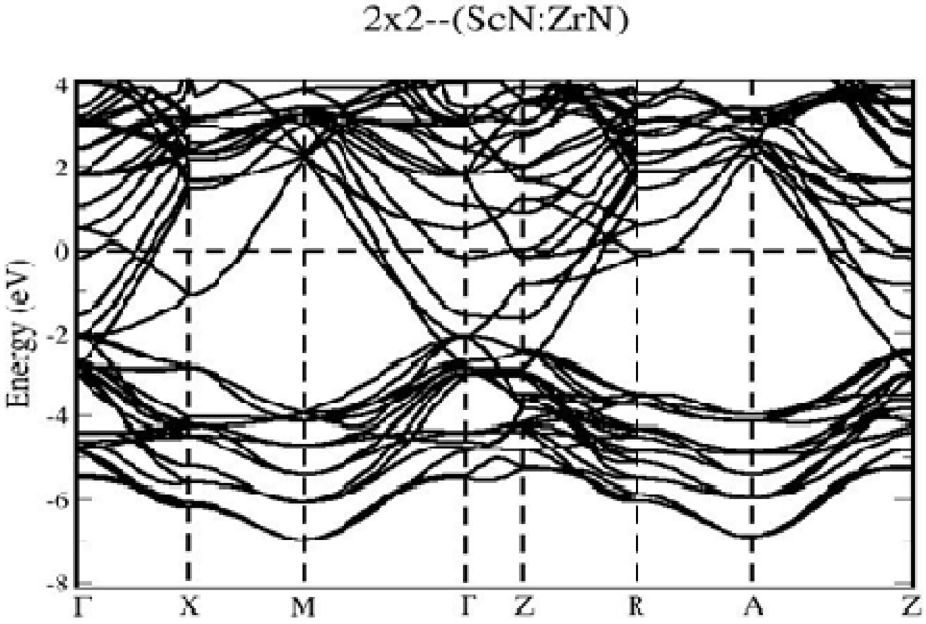

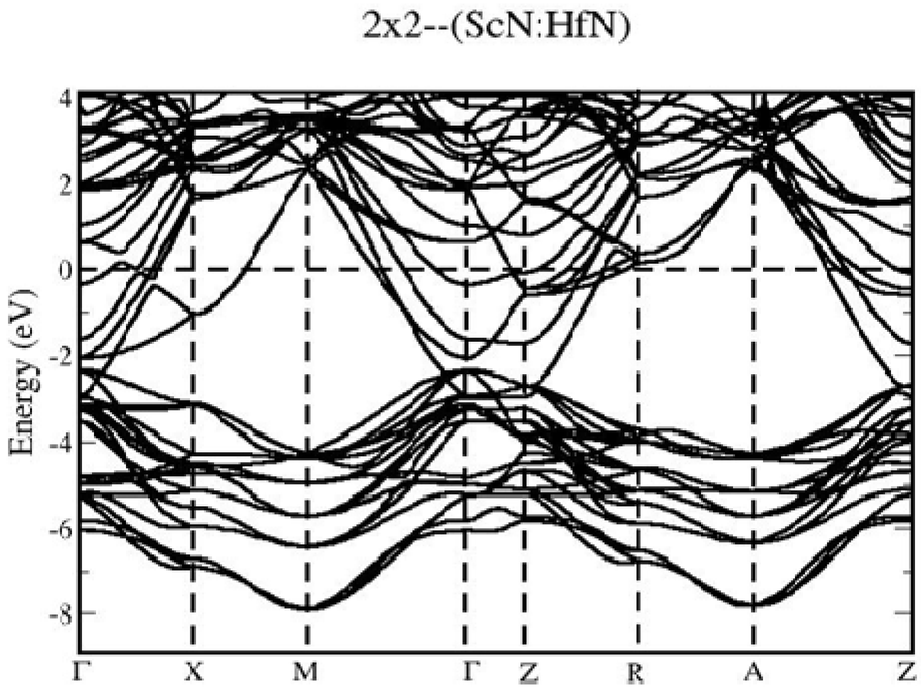

Figure 5(a) Electronic structure of 2/2-ZrN/ScN and (b) 2/2-HfN/ScN metal/semiconductor superlattice along the high symmetry directions of the tetragonal Brillouin Zone. The symmetry points are Γ (0, 0, 0), X (0,$\frac{1}{2}$, 0), M ($\frac{1}{2}$, $\frac{1}{2}$, 0), Z (0,0,$\frac{1}{2}$), R(0, $\frac{1}{2}$,$\frac{1}{2}$), A ($\frac{1}{2}$,$\frac{1}{2}$,$\frac{1}{2}$). Relatively flat band at the Fermi energy along the Γ – Z directions can be observed.

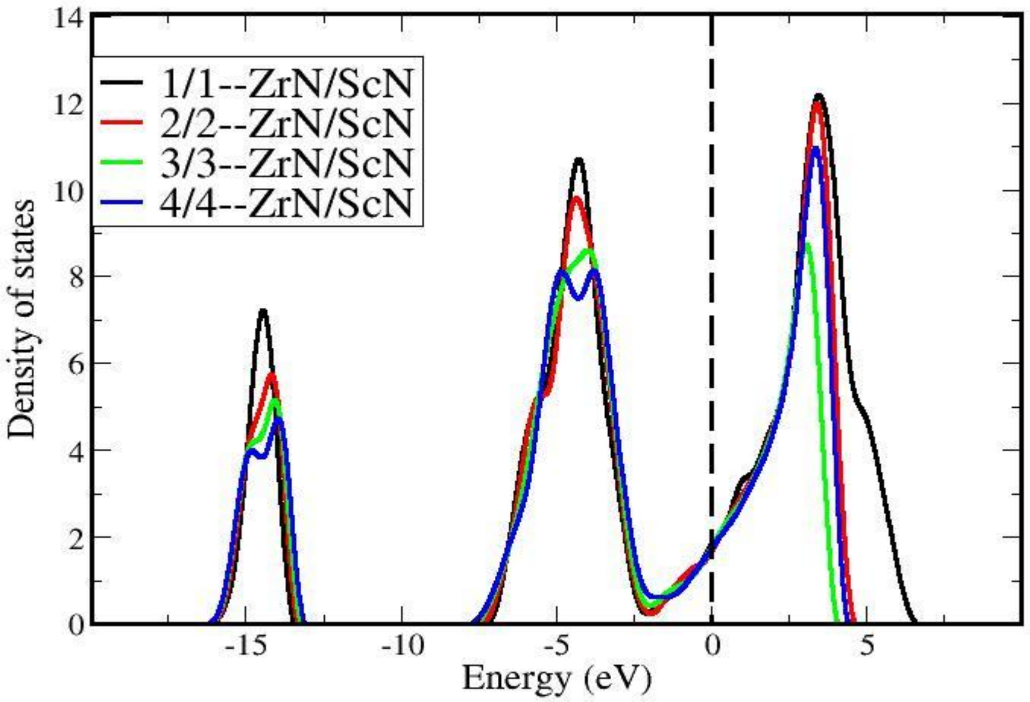

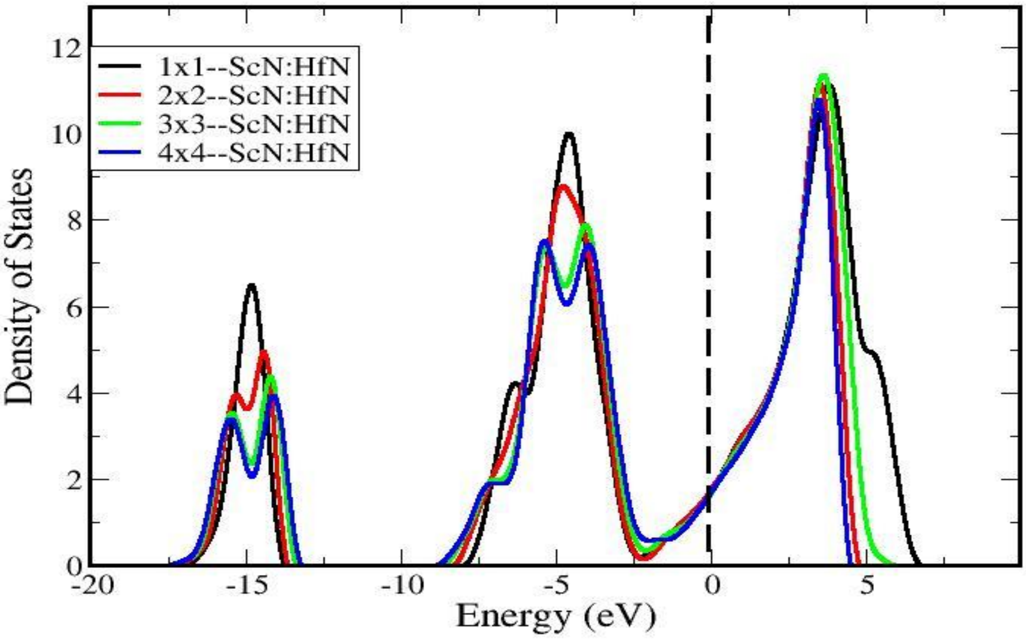

Figure 6(a) Electronic densities of states of the 2/2-ZrN/ScN and (b) 2/2-HfN/ScN metal/semiconductor superlattices. Asymmetric linearly increasing densities of states at the Fermi energy, necessary for increasing thermopower is observed.

Table I. Energy difference between the Fermi energy and the bottom of the Γ-Z-band $_{\text{of}}$ various superlattices showing their extent of degeneracy.

m/n Metal/ScN superlattice	E_{Fermi}-$E_{\Gamma\text{-Z-band}}$ for ZrN/ScN (eV)	E_{Fermi}-$E_{\Gamma\text{-Z-band}}$ for HfN/ScN (eV)
2/2-superlattice	0.169	0.360
3/3-superlattice	0.231	0.342
4/4-superlattice	0.334	0.388
2/4-superlattice	0.301	0.481
4/2-superlattice	0.095	0.250

The extent of their degeneracy is enumerated in Table I. The energy difference between the Fermi energy and the bottom of the Γ-Z valance band suggests that ZrN based superlattices are more degenerate compared to its HfN based counterparts.

To get an insight into the role of electronic structure on the electrical properties of these superlattices, we have visualised the electronic states at the Γ-point of the Brillouin zone for the highest occupied states and the lowest unoccupied states for the 4/4-ZrN/ScN superlattice. The highest occupied electronic states (at the Γ-point) are hybridised Sc *d*-orbital and are largely confined to the ScN layers, while the lowest unoccupied states (at the Γ-point) are localised at the interface between the metal and semiconductor layers. Electronic states between different layers are also weakly coupled to each other resulting lower electrical conductivity across the interface.

The Fermi surface plots of these superlattices are intriguing [see Fig. 8]. Since the electric field driven currents always flow perpendicular to the Fermi surface, the curves indicate low electrical current along the z-direction of these superlattices [with contributions coming from the last 4 surfaces of the Fig 8], while along the in-plane directions the current density should be higher [all the surfaces has contribution to the electric field driven current along the in-plane directions].

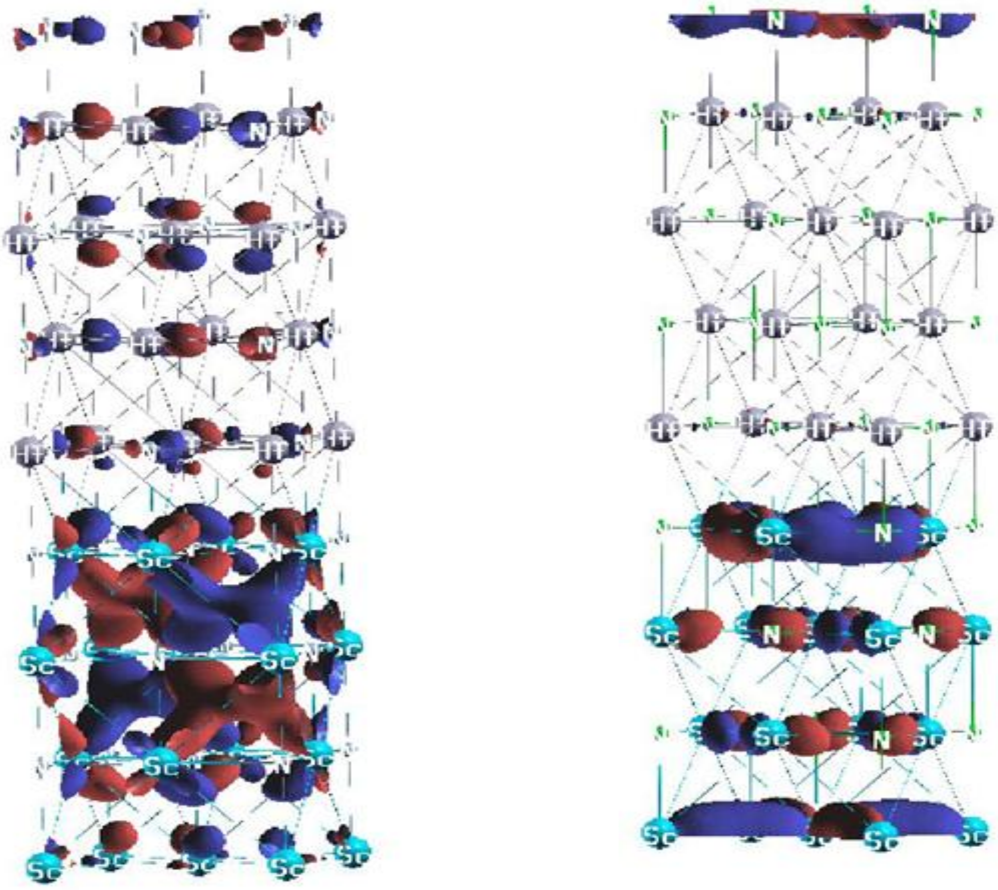

Figure 7(a) Highest occupied and (b) Lowest unoccupied electronic states at the Γ point for 4/4-ZrN/ScN metal/semiconductor superlattice.

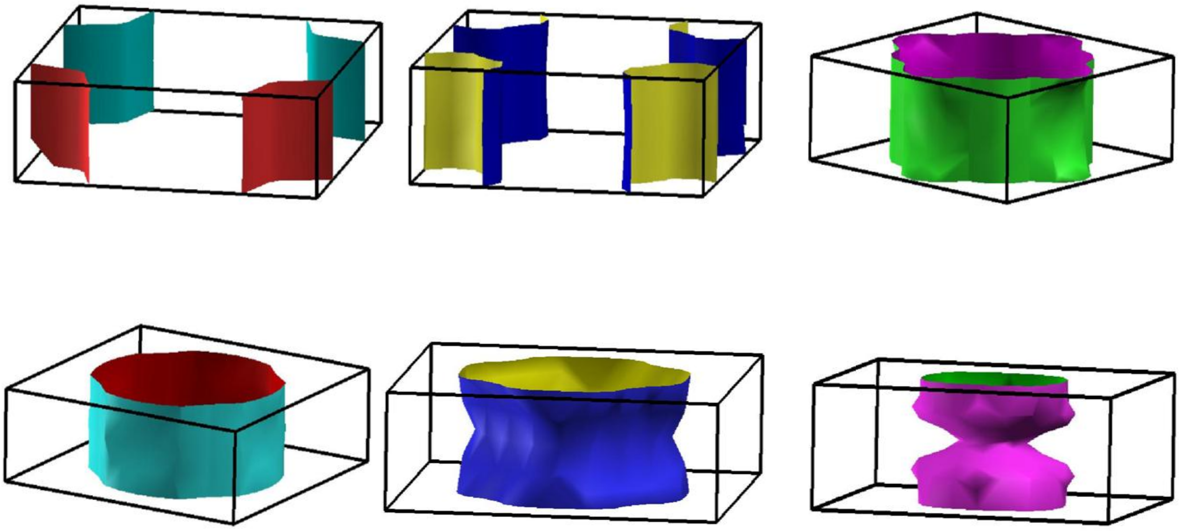

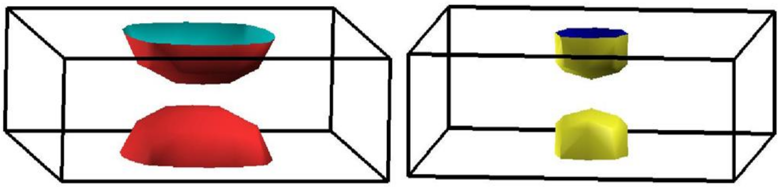

Figure 8 Fermi surfaces of 3/3 ZrN/ScN metal/semiconductor superlattices. The first four surfaces contribute primarily to the electrical current along the in-plane directions, while the next four have contributions along the cross plane directions.

4.3.3 Vibrational Spectra

Vibrational spectra of 2/2 ZrN/ScN and HfN/ScN superlattices [see Fig. 2(a) and 2(b)] reveal a reduction in the velocities of transverse acoustic modes along the growth direction, with a more pronounced effect in the case of HfN/ScN superlattices. Due to the mismatch in the bulk phonon density of states of the component materials, the mid-frequency range optical phonon bands of ScN are flattened along the cross-plane directions (i.e. Γ-Z, R-X, M-A) of the superlattices, making weak contributions to the lattice thermal conductivity along the cross-plane direction. On the other hand, along the in-plane directions (i.e. Γ-X), vibrational

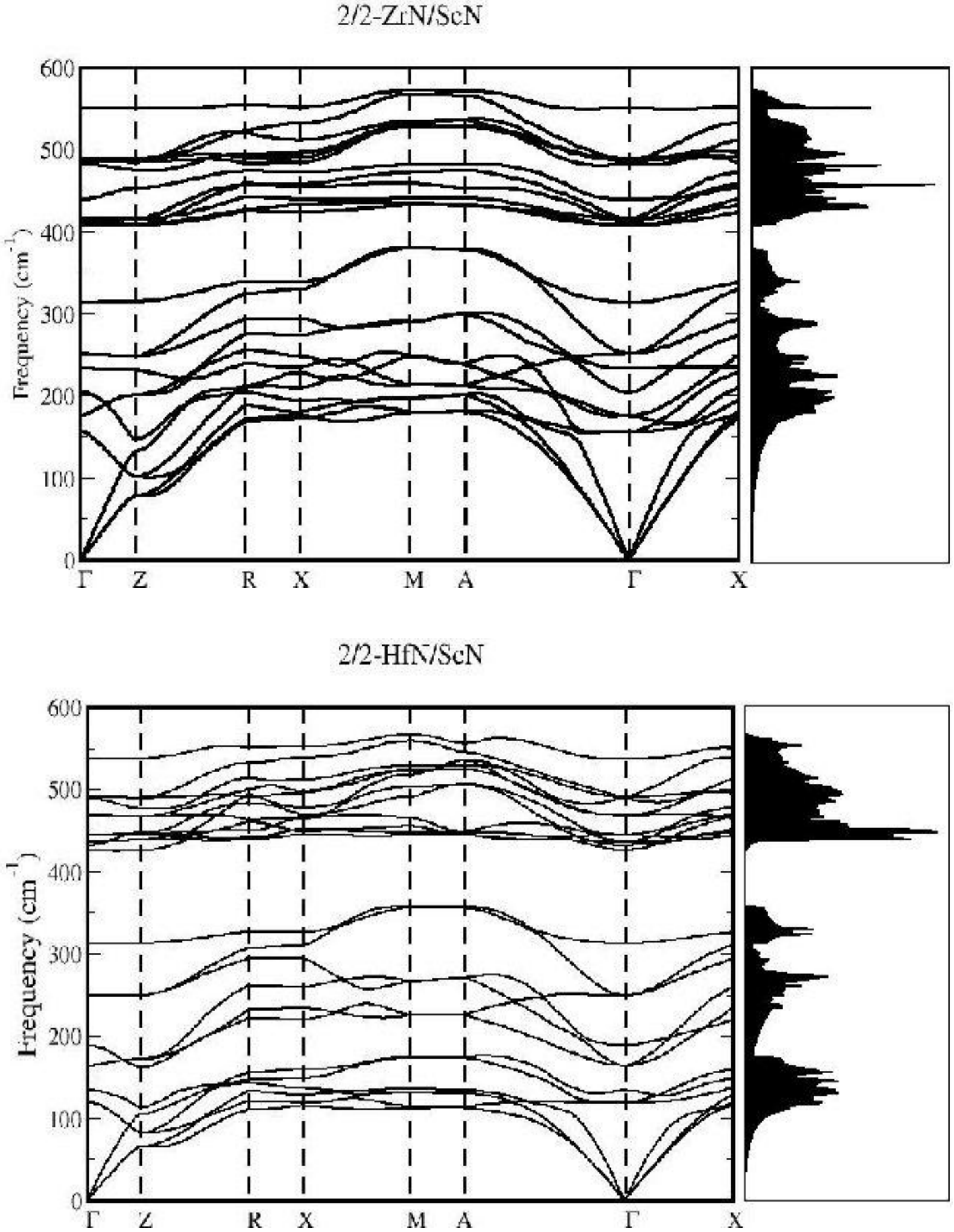

Figure 9(a) Vibrational spectra and phonon density of states of 2/2 ZrN/ScN and (b) 2/2 HfN/ScN metal/semiconductor superlattices. Localised phonons, manifested as flat dispersion along the Γ – Z, R – X, and M - A directions are observed.

modes disperse as steeply as expected from the phonon dispersion of bulk materials.

We have also visualised the displacement patterns of atoms at the Γ-point of the Brillouin zone for various superlattices [see Fig. 10]. The pictures suggest that all the low frequency vibrations arise due to the movement of *Sc*, *Zr*, and *Hf* atoms, while the high frequency vibrations are from the N-atom movement.

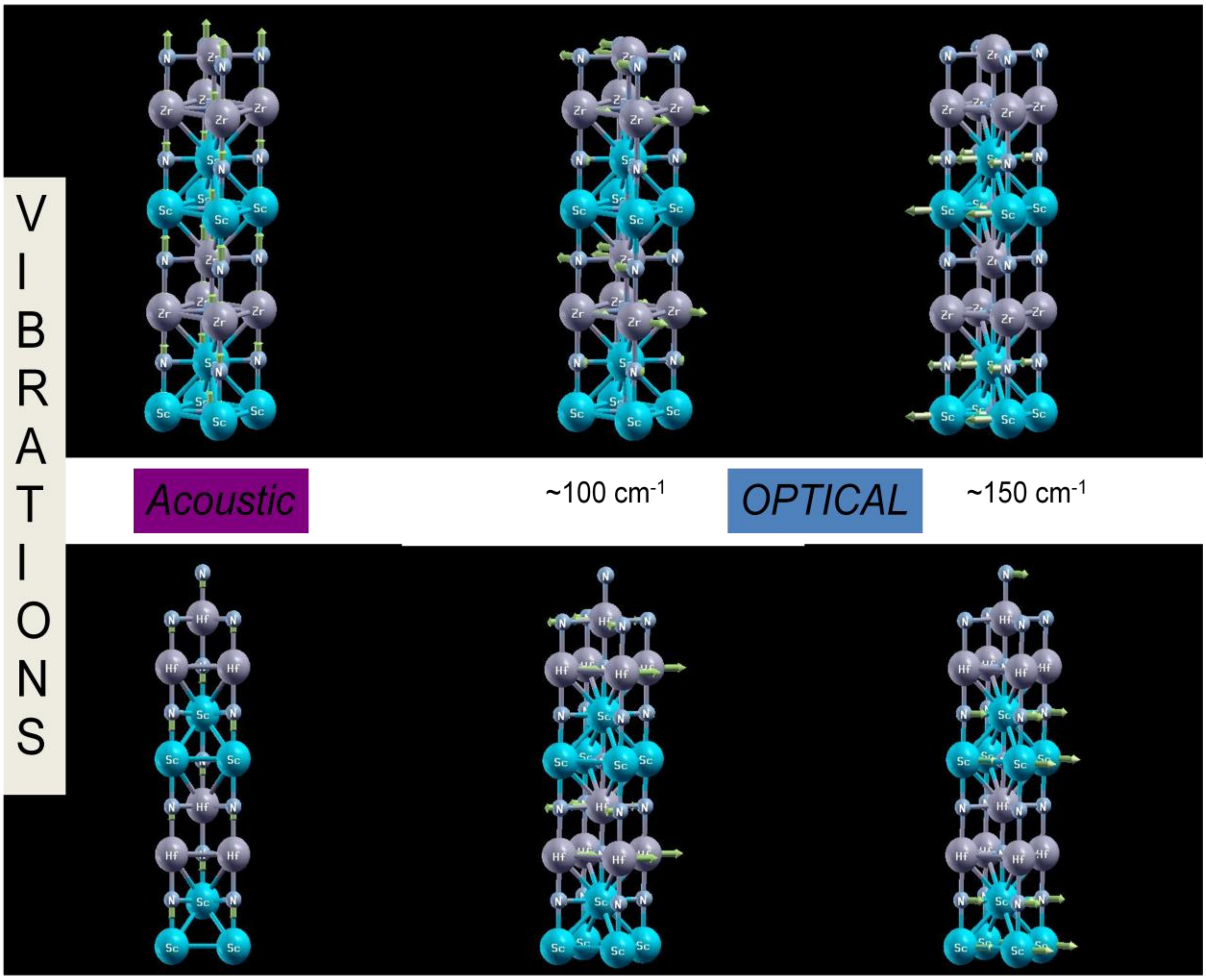

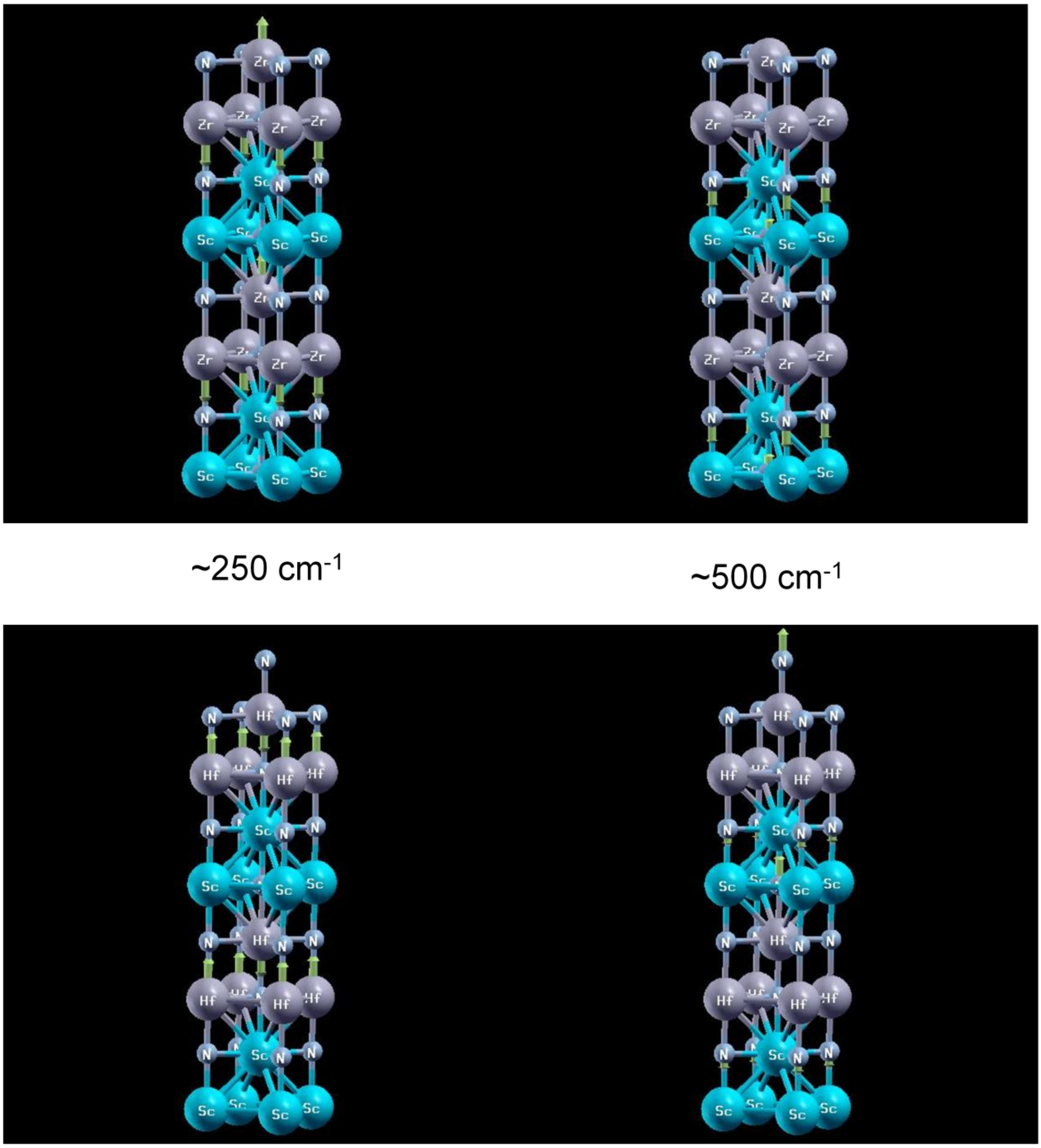

~250 cm^{-1} ~500 cm^{-1}

Figure 10 Displacement patterns of different vibrating atoms for the 2/2-metal/semiconductor superlattices at the Γ-point.

4.3.4 Thermal Properties

We now analyze the lattice thermal conductivity using Boltzmann transport theory. Since we have not determined anharmonic interactions between phonons, it is not possible to estimate scattering times. We assume that scattering times are constant for all phonons and compare thermal conductivity of different superlattices with that of the bulk form of their components, which includes only the effects of densities of states and phonon group velocities. Our estimates of cross-plane lattice thermal conductivity [see Fig 11 (a)] κ for 1/1 superlattices are comparable to the bulk lattice thermal conductivity; while there is almost a 10-fold reduction in κ for 2/2 superlattices compared to the 1/1 case, and to bulk ZrN and HfN values. The extent of reduction is found to be even larger (almost 100 times) with respect to the bulk ScN case, with HfN based superlattices showing overall lower κ than its ZrN-based counterparts due to Hf's larger mass compared to Zr. This large reduction of lattice thermal conductivity can be understood in terms of the phonon filtering effect at the interface, where the mismatch in phonon density of states of the bulk materials prevents ScN mid-frequency range phonons from being propagated across the interface. Smaller κ for HfN based superlattices can also be explained through the comparisons of the bulk phonon density of states where the acoustic branches of HfN are in significantly different frequency range than those of ScN. This huge reduction in cross-plane lattice thermal conductivity makes these superlattices highly efficient for optimising ZT for thermoelectric energy conversion devices. Our estimates of κ are upper bound on κ as the scattering time τ is expected to be smaller for superlattices due to additional scattering at the interfaces, reducing κ even further.

Examination of the temperature variation of cross-plane lattice thermal conductivity reveals the dominance of acoustic phonons at low temperatures [see Fig 11 (b) and 11(c)]; while even at room temperatures optical phonons contribute a significant amount to κ in the case of HfN/ScN superlattices. In ZrN/ScN-based superlattices, a relatively smaller contribution of optical phonons to κ is observed resulting from the lower group velocity of the optical phonons, as many optical phonons of ZrN are located in the small gap of ScN optical phonons at around the 500 cm^{-1} frequency range.

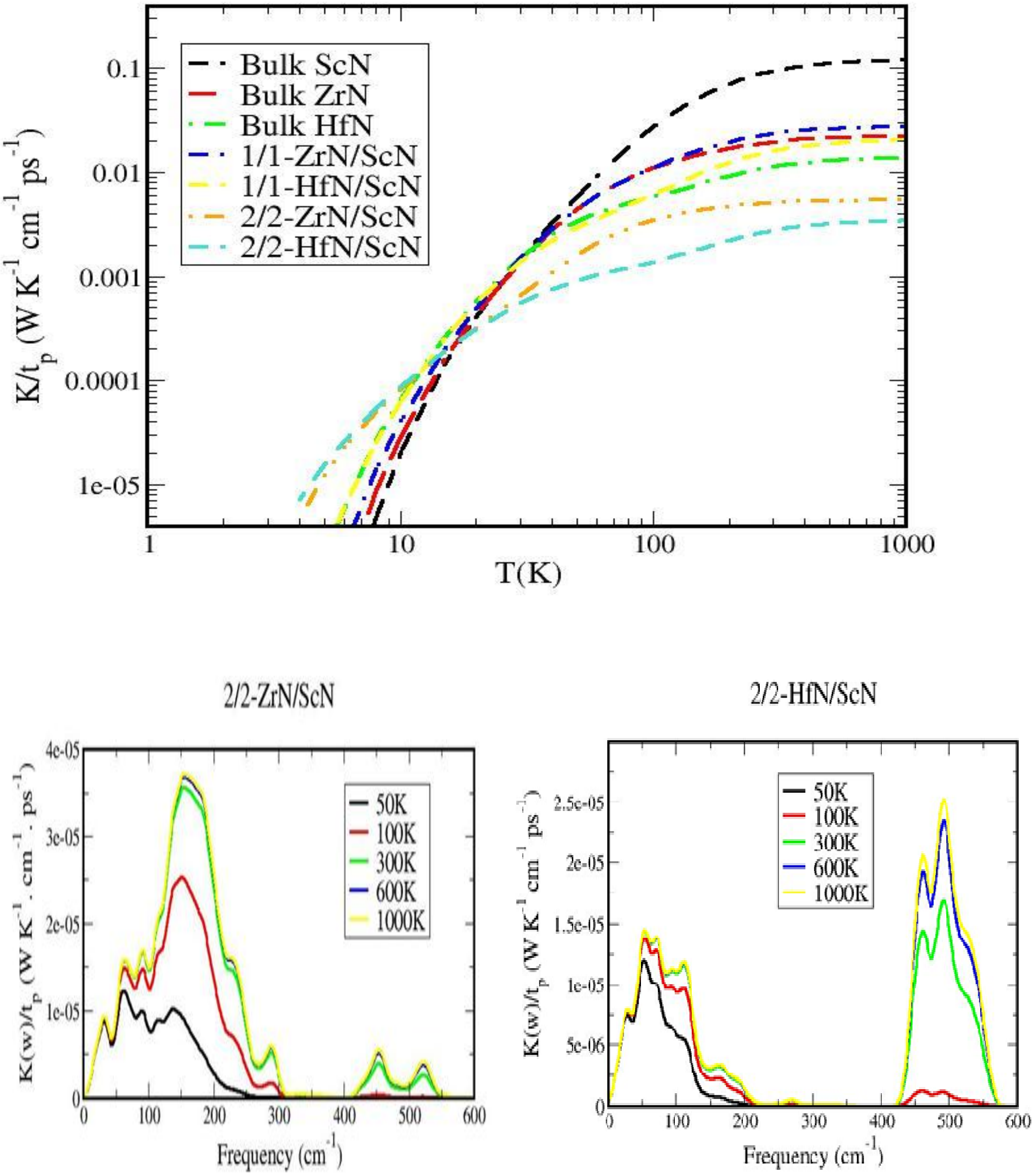

Figure 11(a) Boltzmann transport based calculations of cross-plane lattice thermal conductivity for bulk materials and superlattices, representing reduction of κ along the cross-plane direction. (b) and (c) cross-plane lattice thermal conductivity as a function of phonon frequencies at different temperatures.

4.4 Conclusions

In summary, we have determined electronic structure, vibrational spectra and thermal properties of ZrN/ScN and HfN/ScN metal/semiconductor superlattices from first-principles calculations. Our results show presence of asymmetry in electronic DOS, and flattening of bands near the Fermi energy along the cross-plane direction of these superlattices, which is expected to result in enhancement of Seebeck coefficient along the growth direction. Analysis of vibrational spectra and Boltzmann transport theory based calculations show a large reduction in lattice thermal conductivity along the cross-plane direction of these superlattices with respect to their individual bulk components as the phonons are filtered at the interfaces due to mismatch in the bulk vibrational spectra. Understanding of the metal/semiconductor superlattices and their properties developed here should be useful in design of nano-structured superlattices with excellent thermoelectric performance.

References

1. A. J. Minnich, M. S. Dresselhaus, Z. F. Ren and G. Chen, Energy and Environmental Science, 466, **2** (2009).

2. J. Baxter et al, Energy and Environmental Science, 559, **2** (2009).

3. J. Androulakis, C. H. Lin, H. J. Kong, C. Uher, C. I. Wu, T. Hogan, B. A. Cook, T. Caillat, K. M. Paraskevopoulos and M. G. Kanatzidis, J. Am. Chem. Soc., 9780, **129** (2007).

4. J. P. Heremans, V. Jovovic, E. S. Toberer, A. Saramat, K. Kurosaki, A. Charoenphakdee, S. Yamanaka and G. J. Snyder, Science, 554, **321 (**2008).

5. L. D. Hicks and M. S. Dresselhaus, Phys. Rev. B, 16631, **47** (1993).

6. L. D. Hicks and M. S. Dresselhaus, Phys. Rev. B, 12727, **47** (1993).

7. T. C. Harman et al, Science, 2229, **297 (**2002).

8. R. Venkatasubramanian, E. Siivola, T. Colpitts, B. O'Quinn, Nature, **597** (2001).

9. A. Shakouri and J. E. Bowers, Appl. Phys. Lett., 1234, **71** (1997).

10. D. Vashaee and Ali Shakouri, Phys. Rev. Lett., 106103, **92** (2004).

11. M. Zebarzadi, Z. Bian, R. Singh, A. Shakouri, R. Wortman, V. Rawat, T. D. Sands, Journal of Electronic Materials, 960, **38** (2009).

12. G. Zeng, J. E. Bowers, J. M. O. Zide, A. C. Gossard, W. Kim, S. Singer, A. Majumdar, R. Singh, Z. Bian, Y. Zhang and A. Shakouri, Appl. Phys. Lett., 113502, **88** (2006).

13. Z. Bian and A. Shakouri, Appl. Phys. Lett., 012102, **88** (2006).

14. V. Rawat, Y. K. Kho, D. G. Cahill, T. D. Sands, Journal of Applied Physics, 024909, **105** (2009).

15. Bivas Saha, Jagaran Acharya, Timothy D. Sands and Umesh V. Waghmare, Journal of Applied Physics, 033715, **107** (2010).

16. J. P. Perdew, K. Burke, and M. Ernzehof, Phys. Rev. Lett., 3865, **77** (1996).

17. Vanderbilt, Phys. Rev. B, 7892, **41** (1990).

18. H. J. Monkhorst and J. D. Pack, Phys. Rev. B, 5188, **13** (1976).

19. M. Methfessel and A. Paxton, Phys. Rev. B, 3616, **40** (1991).

20. V. I. Anisimov and O. Gunnarson, Phys. Rev. B, 757, **43** (1991).

21. S. Baroni, S. D. Gironcoli, A. D. Corso, P. Giannozzi, Rev. Mod. Phys., 515, **73** (2000).

22. G. Mahan and Sofo, PNAS, 7436, **93 (**1996).